

A proposed paper submitted to
Applied Energy

**Impacts of urban morphology on improving urban wind energy potential
for generic high-rise building arrays**

Yu-Hsuan Juan ^{a, b}, Chih-Yung Wen ^c, Zhengtong Li ^c, An-Shik Yang ^{b, d*}

^a Department of the Built Environment, Eindhoven University of Technology, Eindhoven, The Netherlands

^b Department of Energy and Refrigerating Air-Conditioning Engineering, National Taipei University of Technology, Taipei 106, Taiwan

^c Department of Mechanical Engineering and Interdisciplinary Division of Aeronautical and Aviation Engineering, The Hong Kong Polytechnic University, Kowloon, Hong Kong

^d Research Center of Energy Conservation for New Generation of Residential, Commercial, and Industrial Sectors, National Taipei University of Technology, Taipei 106, Taiwan

Corresponding author:

Dr. An-Shik Yang (Corresponding Author)
Distinguished Professor and Department Chairman
Department of Energy and Refrigerating Air-Conditioning Engineering
National Taipei University of Technology
1, Sec. 3, Chung-Hsiao E. Rd., Taipei 106, Taiwan, R.O.C.
Tel: (886) 2-2771-2171 ext. 3523
Fax: (886) 2-2731-4919
Email: asyang@ntut.edu.tw

Abstract

Urban wind energy has been beneficial for the sustainable development of cities over these years. With the increasing popularity of utilizing CFD techniques, it has been attracting public attention to the layout of urban morphology for achieving the most sustainable form in progressing urban wind development for the future. This study aims to assess urban wind energy with a view of urban morphology. The wind energy potential results around the 6×6 arrays of generic high-rise buildings are analyzed by the urban morphology parameters, including (i) urban density altered from very compact (λ_p of 0.76) to sparse urban layouts (λ_p of 0.09), (ii) building corner shapes of sharp and rounded corners, (iii) urban planning of in-line and staggered layouts, and (iv) wind directions of 0° and 45°. This investigation implements the three-dimensional (3D) steady Reynolds-averaged Navier-Stokes (RANS) equations with the Reynolds stress model (RSM) to explore the distributions of wind speed, wind power density, and turbulence intensity around high-rise buildings. The results indicate that decreasing λ_p can reduce the unacceptable turbulence areas with relatively higher wind power density on the roof. In addition, round corners for a sparse urban layout of $\lambda_p = 0.09$ show the highest power densities up to 201% and 150% greater than those of sharp corners for two selected areas both beside the building and on the roof, respectively. Even under the oblique wind direction of 45°, the rounded corner still shows better wind energy potentials than the sharp corner. The in-line urban layout produces more significant areas with higher power densities and low turbulence intensities than those of the staggered urban layout.

Keywords: Urban wind energy; urban morphology; wind resource assessment; high-rise building; urban density; aerodynamic modification.

1. Introduction

Urban wind energy presents lots of interest through turbine installation in the urban environment, which can solve the transportation difficulties of electric transmission lines from the wind farms in remote locations to cities [1, 2]. However, the challenges are also caused by complicated interactions of turbulent wind flows and eddies with urban forms and structures [3]. The urban morphology is usually directly related to the characteristics of urban environments, including the urban density and urban arrangement, and the geometry of buildings. Consequently, to maximize the urban wind energy potential for facilitating sustainable urban areas at the neighborhood and city scales, it is crucial to comprehend the detailed airflow patterns and turbulence characteristics around buildings in the urban configuration. Different flow regimes over street canyons determine the amounts of power density and turbulence intensity around high-rise buildings in urban areas, which are the most essential parameters in the estimation of wind energy potential.

Much attention has been devoted to investigating the relationship between the urban form and sustainability, pinpointing the implications of the shape and density of cities for future progression. Strong arguments from many studies suggest the compact city as the most sustainable urban form [4]. Urban density determines the compactness among buildings, which can be correlated with the urban plan area density (λ_p) (i.e., the ratio between the plan area of buildings viewed from above and the total floor area) and frontal area density (λ_f) (i.e., the ratio of the frontal area of buildings to the total floor area). The building area and frontal area densities are closely linked to the size and shape of buildings. High-rise buildings surrounded by narrow street networks can generally provide high wind speeds at higher altitudes but strong resistance to the approaching wind. In addition, the placement and urban layout design are of major significance. The in-line or staggered building arrangements are also crucial in determining whether it is profitable for turbine installation. Escalating urban airflows in high-rise compact urban areas may enhance the urban wind energy potential between the urban canopy layers and their surroundings. A study on the interactions of the turbulent wind flows with buildings in such urban areas can be very useful to formulate the guidelines of better urban wind power implementation strategies in urban planning.

As an effective tool for the early-stage urban design and planning, computational fluid dynamics (CFD) simulations were conducted to achieve the parametric studies of outdoor wind environments affected by the urban morphology [5, 6]. The prediction capabilities were verified via the wind tunnel measurements [7-9] or on-site measurements [10-12] to ensure reasonable calculation accuracy. Existing investigations of urban morphology primarily focused on the comprehension of urban ventilation [13-16], pedestrian wind comfort [17-20], urban heat island [21, 22], energy consumption [23-25], air pollution [26-29] and wind load distribution [30, 31]. Urban wind energy potential has been a newly developing related topic in the past decade [32-36]. The parametric studies of generic urban configurations simplify actual complex urban geometries into generic simple morphological models, extensively used in the analyses of urban wind environments for their advantages of linking specific geometric parameters to urban wind energy outcomes. Up to now, most studies of urban wind energy

potential have dealt only with one cuboid [7-9, 37-39], or two parallel buildings [40, 41]. Only limited papers examined the wind field around cube arrays (i.e., $H/W=1$) [6, 42], or low-rise building arrays with aspect ratios of less than 2 [43]. As exponential growth of high-rise buildings combined with mass urbanization, the high-rise urban areas as the future trend still lack the knowledge-based expert technique for the initial estimation of urban wind power potential at promising locations for turbine installation. Some earlier studies like Lu and Ip [44] and Ledo et al. [42] were focused on the influence of sharp roof shapes (i.e., pitched, pyramidal, and flat roofs) on the distributions of wind speed and turbulence intensity. Wang et al. [45] examined the configurations of two perpendicular buildings with different building dimensions, corner separation distances, and angles. Balduzzi et al. [46] investigated the effects of the installation building height, the height and width of its upwind building, and the distance between the buildings themselves on the flat or sloping roofs for five buildings. Millward-Hopkins et al. [43] proposed the effective access of the highest wind resource available for a uniform array by increasing the mounting height on the roof with further arranging the mounting point close to the leading edge. Heath et al. [47] analyzed the wind field around a simple pitched-roof building on a 6x4 cube array to determine the optimum mounting sites for varied prevailing wind directions. To extend the investigations to other shapes of aerodynamic modifications, Abohela [48] explored the vaulted roofs with better advantage over an isolated building than a 5x5 cube array. Toja-Silva et al. [6] performed a CFD analysis for various shapes to suggest a spherical roof with a cylindrical wall optimized for wind energy utilization. Zhou et al. [40] identified that the composite prism building shape has huge wind energy potential between two low-rise buildings. From the aforementioned literature survey, a systematic study on the urban wind power potential over various possible locations around the building is still incomplete. Most researches only focus on the locations over the building roof [6, 32, 42, 46, 48]. Some studies have indicated other suitable installation sites, such as along the passage between buildings [40, 41], on the side of the building [7], or directly integrated into the building [35]. Few studies considered harvesting wind energy in comprehensive regions around the whole urban areas [10, 12]. To attain a better understanding of the design approaches of urban morphology for enhancing wind energy harvesting, it is therefore worthy of investigating the wind power potential in high-rise building arrays to bridge the knowledge gap between urban morphology parameters and wind field performance for practical urban design applications.

In this study, the parametric scenarios of generic urban configurations are defined in a practical manner. For high-rise densely populated cities like Hong Kong and the Manhattan district in New York, buildings are generally tall with relatively narrow streets (as shown in Fig. 1). The street aspect ratio (the ratio of building height to street width, H/W) in the main urban area of Hong Kong is commonly more than 2–4, somewhere even up to 6–10. Hence, λ_p usually ranges from 0.25 to 0.4, or arrives at 0.5 or more in some special circumstances. In this context, the objective of this paper is to examine the influences of typical urban density variations on wind energy potential, which have been rarely investigated. To investigate the wind energy harvesting for high-rise building arrays in a compact city, the research purposes of this study consist of the following tasks.

- 1) A regular 6×6 high-rise building array layout is set up as the object for full-scale CFD simulations, with the urban density varied from a very compact urban layout ($\lambda_p= 0.76$ and $\lambda_f= 3.4$) to a sparse urban layout ($\lambda_p= 0.09$ and $\lambda_f= 0.43$), to quantify the effects of urban morphology variations on the wind power density and turbulence intensity.
- 2) The replacement of sharp corners with round corners for all building and roof edges in the center 2×2 high-rise buildings array is implemented to enhance wind energy potential as one of the effective aerodynamic modifications.
- 3) The CFD simulations are conducted to compare the wind power potentials around the staggered building layouts at varied urban densities with those around the regular in-line building layouts.
- 4) The wind energy resources for two incident wind directions $\theta= 0^\circ$ and 45° are investigated.
- 5) Two areas, including (i) beside the sidewall of buildings and (ii) above the roofs for possible wind turbine installation, are selected to characterize the wind flow field around the building arrays at varied design parameters.

This paper is systematized as follows: The predictions are compared with wind tunnel measurements for the CFD validation study, as illustrated in Sec. 2. Sec. 3 describes the CFD simulation details, consisting of all case scenarios, the computational domain, grid, settings, and grid-sensitivity analysis. In Sec. 4, the CFD simulations present the results of four impacts: (i) the urban density, (ii) the building corner shape, (iii) urban layout, and (iv) the wind direction on the evaluation of wind power potential. The limitations in the current study are discussed in Sec. 5. Sec. 6 summarizes the main conclusions obtained.

2. CFD validation study

The wind-tunnel experiments are performed using an open-circuit atmospheric boundary layer wind tunnel of Eindhoven University of Technology (TU/e). The cross-section of the wind tunnel is 0.5 m × 0.65 m with 13 m long. A set of floor roughness elements is located 0.65 m ahead of the test section to reproduce the atmospheric boundary layer. The test model consists of four square cuboids placed as a 2×2 building array with a straight crossing street-canyon width of 0.028 m. The dimensions of the square cuboid model are 0.031 m × 0.031 m × 0.14 m, resulting in a blockage ratio of 3% in the wind tunnel with a scale of 1:643. The turbulent flow instrumentation (TFI) Cobra probe is utilized to measure the 3-component flow velocities and turbulence intensities [49]. Fig. 2a shows the locations of monitoring points on the lateral view of 6 profiles along the vertical centerlines ($y/B = 0$) at 6 positions ($x/B = -2.9, -1.94, -0.97, 0, 0.97$ and 1.94). The dimensionless incident vertical profiles (Fig. 2b) of time-averaged streamwise velocity (u/u_{ref}) and total turbulence intensity (TI/TI_{ref}) are measured from the empty wind tunnel, which are readily employed in CFD validation. The values of u_{ref} and TI_{ref} are 13.4 m/s and 8% at the building height.

The overall computational domain for the reduced-scale CFD validation study is depicted in Fig. 2c, following the CFD best practice guidelines [50, 51]. The high grid resolution computational mesh is generated using hexahedral elements only, with a total number of 5,464,450 cells. No less than 20 cells

are disposed along with the passage distance between the crossing street canyons. A peak stretch factor of 1.1 is adopted with the least cell volume of $2.7 \times 10^{-9} \text{ m}^3$ to ensure y^* values within 30 and 350 for proper implementation of the standard wall function treatment. For the boundary conditions, the solid walls are arranged as the no-slip walls, whereas the ground surfaces integrate the sand-grain roughness modification with the roughness height (k_s) of 0.0007 m and the roughness constant (C_s) of 0.13. To realize the roughness in the wind-tunnel tests, the aerodynamic roughness length z_0 is set as 9×10^{-6} m. The outlet boundary is specified to be 1 atm. The lateral and top boundaries are imposed as symmetry with zero normal velocity and zero normal gradients of flow variables. The grid-sensitivity analysis has checked the suitability of grid resolution. The CFD validation study utilizes the ANSYS/Fluent v19 to perform the 3D Reynolds-Averaged Navier-Stokes (RANS) simulations. As the most elaborate turbulence model provided by ANSYS/Fluent, the Reynolds stress model (RSM) turbulence model is selected based on a turbulence model sensitivity analysis presented in Sec. 2.1. In effect, RSM solves seven transport equations as turbulence closures to determine the individual components of the Reynolds stress tensor. The second-order discretization scheme is implemented in CFD calculations for the convection and diffusion terms of the governing equations. An iterative semi-implicit method for pressure-linked equations (SIMPLE) algorithm is used for the pressure-velocity coupling [34, 35]. All the normalized residual errors of continuity, momentum, k , and ε equations are converged to 10^{-6} for attaining a steady solution.

2.1. Turbulence model sensitivity analysis

The sensitivity analysis is performed to evaluate the prediction capabilities of the standard k - ε model (SKE) [52], the realizable k - ε model (RKE) [53], the renormalization group k - ε model (RNG) [54], the shear-stress transport k - ω model (SST) [55] and the RSM model [56]. Figure 3a presents a comparison of u/u_{ref} against the wind-tunnel measured data along the vertical centerline ($y/B = 0$) at $x/B = -2.9, -1.94, -0.97, 0, 0.97$ and 1.94). Overall, the agreement of u/u_{ref} between all five models and wind-tunnel measurements is acceptable in front of the four square cuboids ($x/B = -2.91$ and -1.94). For the other four positions, RSM has the best agreement with the wind-tunnel data, with the mean absolute differences less than 5%.

Figure 3b presents a comparison of TI/TI_{ref} against the measured data at the aforementioned six positions. It is clear that the SKE, RKE, RNG, and SST models unsatisfactorily predict the turbulence intensities. Nevertheless, only the RSM model can reproduce the turbulence intensity profiles with the absolute mean differences less than 16%. Thus, RSM successfully predicts the velocity and turbulence intensity fields.

3. CFD simulation

3.1. Description of urban scenarios

This study examines four different impacts of urban morphologies on the development of urban wind energy. The arranged scenarios of generic urban layouts dispose the urban geometric parameters

from practical applications. Table 1 illustrates the details of all involved parameters and investigated values in CFD simulation cases, as depicted in Fig. 4. All cases are based on a 6×6 array of identical high-rise buildings in the full-scale dimensions. Each high-rise building has the same building height (H) of 90 m and an equal building length (B) of 20 m with different street canyon widths (W). The street canyon width between the buildings from the highest to lowest density cases are varied from 0.15B to 2.25B. To study the variation of urban density, two key parameters, urban plan area density (λ_p) and frontal area density (λ_f), are adopted and defined by Oke [57] in Fig. 4. Table 1 illustrates the details of 18 simulation cases to elucidate the influences of urban morphologies on urban wind energy as the following four parameters:

- (1) Urban density: W varied from 0.15B to 2.25B, corresponding to the transformation from a very compact urban layout ($\lambda_p= 0.76$ and $\lambda_f= 3.4$) to a sparse urban layout ($\lambda_p= 0.09$ and $\lambda_f= 0.43$).
- (2) Building corner shape: Comparison of wind power potential between the sharp and rounded building corner shapes. The rounded corners are implemented on only the central 2×2 array of four high-rise buildings, as shown in Fig. 5 in gray color, while others are maintained as sharp corners. Here the radius of rounded corner modifications of building and roof corners is 0.15B.
- (3) Urban layout: Both the regular in-line and staggered urban layouts are investigated at varied urban densities.
- (4) Wind direction: Two wind directions of 0° and 45° are performed.

Table 1 Details of involved parameters for CFD simulation cases.

<i>Case name</i>	<i>Street canyon width, W/B</i>	<i>Urban plan area density</i>	<i>Frontal area density</i>	<i>Urban layout</i>	<i>Corner shape</i>	<i>Wind direction</i>
A1	0.15	0.76	3.40	In-line	Sharp	0°
A2	0.3	0.59	2.66	In-line	Sharp	0°
A3	0.45	0.48	2.14	In-line	Sharp	0°
A4	0.75	0.33	1.47	In-line	Sharp	0°
A5	1	0.25	1.13	In-line	Sharp	0°
A6	2.25	0.09	0.43	In-line	Sharp	0°
B1	0.15	0.76	3.40	In-line	Rounded	0°
B2	0.3	0.59	2.66	In-line	Rounded	0°
B3	0.45	0.48	2.14	In-line	Rounded	0°
B4	0.75	0.33	1.47	In-line	Rounded	0°
B5	1	0.25	1.13	In-line	Rounded	0°
B6	2.25	0.09	0.43	In-line	Rounded	0°
C1	0.5	0.4	2	Staggered	Sharp	0°
C2	1	0.25	1.13	Staggered	Sharp	0°
C3	0.5	0.4	2	Staggered	Rounded	0°
C4	1	0.25	1.13	Staggered	Rounded	0°
D1	0.15	0.76	3.40	In-line	Sharp	45°
D2	0.3	0.59	2.66	In-line	Sharp	45°
D3	0.45	0.48	2.14	In-line	Sharp	45°
D4	0.75	0.33	1.47	In-line	Sharp	45°
D5	1	0.25	1.13	In-line	Sharp	45°
D6	2.25	0.09	0.43	In-line	Sharp	45°

D7	0.15	0.76	3.40	In-line	Rounded	45°
D8	0.3	0.59	2.66	In-line	Rounded	45°
D9	0.45	0.48	2.14	In-line	Rounded	45°
D10	0.75	0.33	1.47	In-line	Rounded	45°
D11	1	0.25	1.13	In-line	Rounded	45°
D12	2.25	0.09	0.43	In-line	Rounded	45°

3.2. Computational domain and grid

The extent of the computational domain from the building array border to the top, lateral, inlet, and outlet boundaries of the computational domain covers 4H, 4H, 4H, and 15H, respectively, following the requirements of the CFD best-practice guidelines [50, 58]. The details of the high-resolution and high-quality computational mesh for Case A4 are depicted in Fig.6, with the magnification of grids near the roof and ground. The minimum cell volume in canyons is $5.5 \times 10^{-3} \text{ m}^3$ in the streamwise, lateral and vertical directions. The grid size is enlarged from the border of high-rise building arrays to the boundaries of the computational domain with an expansion ratio below 1.1. This study arranges the distances from the center points of near-wall cells to the building and ground surfaces below 0.3 m (i.e., the y^+ values ranging from 30 and 500) to ensure effective implementation of the standard wall functions in CFD computations. The total grid numbers for all cases vary approximately 18-26 million, consisting of the hexahedral and prismatic cells only.

3.3. Computational settings

The neutral atmospheric boundary layer inflow profiles of mean wind velocity, turbulent kinetic energy, and turbulence dissipation rate are prescribed at the inlet [93].

$$U(z) = \frac{u^*}{\kappa} \ln \left(\frac{z + z_0}{z_0} \right), \quad (1)$$

$$k(z) = 3.3u^{*2}, \quad (2)$$

$$u^* = \frac{\kappa U_h}{\ln \left(\frac{h + z_0}{z_0} \right)}. \quad (3)$$

Here the aerodynamic roughness length (z_0) is 1 m for treating the surroundings of studied high-rise buildings in a densely built-up area by the updated Davenport-Wieringa roughness classification [94]. The friction velocity (U_h) is 5m/s at the height of 10 m, while the reference wind speed (U_{ref}) of 9.4 m/s at the reference height of 90 m. The standard wall functions with roughness modifications are employed on the ambient ground with the associated roughness height k_s of 0.15 and roughness constant C_s of 8, respectively. All CFD simulations are performed by the 3D steady RANS equations with the RSM model. No-slip boundary conditions and the standard wall functions are implemented to the building surfaces. The zero-gauge static pressure is set at the outlet surface of the computational domain, while the symmetric conditions are imposed on the top and lateral surfaces. All the normalized residual errors of

flow variables converge to 10^{-6} with the mass balance check under 1% to attain the steady wind field environments.

3.4. Grid-sensitivity analysis

The grid-sensitivity analysis is checked by the RSM model for the Case A2 with rounded corners. The simulations of coarser and finer grids are carried out to improve the mesh with a linear refinement factor of $\sqrt{2}$, varying the associated spatial resolutions of grids. The total numbers of mesh system for the coarse, base, and fine grids are 18,644,338, 37,524,060, and 43,130,680 cells, respectively. Figure 7 illustrates the predicted dimensionless streamwise velocity component along the centerline of the building array at $z/H = 0.93$ near the roof for the coarse, base, and fine grids of Case A2. The average deviations of dimensionless streamwise velocity between the coarse and base grids along the centerlines are 4%, whereas the discrepancies are less than 0.5% between the fine and base grids. Therefore, the base grid is retained for the rest of CFD calculations to assess urban wind energy potentials in different cases.

4. Results

In this study, the predictions of wind velocity, wind power density (PD), and turbulence intensity (TI) have been fully investigated to characterize the wind power potential distribution around high-rise building arrays. PD is computed as:

$$PD = \frac{1}{2} \rho V^3 \quad (4)$$

Here V is the velocity magnitude, whereas ρ is the air density. PD is normalized by the reference incident power density, specifically, $PD_{ref} = 508.7 \text{ W/m}^2$ at the building height. Another important factor is turbulence intensity, which is of great interest as the threshold to prevent equipment damages during turbine operations. The limit of reference turbulence intensity (I_{ref}) is prescribed as the classes of wind turbines derived from the International Electrotechnical Commission (IEC) Standard 61400-1 [59]. This is also the representative value of hub-height turbulence intensity at a mean wind speed of 15 m/s averaged over a time of 10 min for a function of turbine class, expressed as below:

$$I_{ref} = TI \left(0.75 + \frac{5.6}{V} \right). \quad (5)$$

The values of I_{ref} of 0.16, 0.14, and 0.12 are categorized into Class A, B, and C of small wind turbine classification based on the IEC standards. This study adopts I_{ref} of 0.16 for Class A wind turbine as the threshold of the acceptable turbulence level for turbine installation [34]. To investigate the effects of the high-rise building array layout on wind energy harvesting, the general possible areas of deploying wind turbines are: (i) mounted on the rooftop, (ii) placed between two adjacent buildings, (iii) located beside the sidewall of buildings. The presence of high-rise building array within the free stream causes two outcomes, which are the high power densities from accelerated airflow speeds and the appropriate reference wind turbulence intensity in the vicinity of high-rise buildings.

4.1. Impact of urban density

Figure 8 illustrates the predicted contour plots of dimensionless velocity magnitude V/V_{ref} (with superimposed streamlines) over the horizontal x-y planes (a) the high-level buildings and (b) above the roofs as well as the vertical x-z planes (c) beside the building sidewalls and (d) along the middle of building column above the roofs for the urban layouts of $\lambda_p = 0.76, 0.25, 0.09$ and the normal wind direction of 0° . Those specific planes are used to characterize the wind flow field around the building array, with the special attention to those installable areas limited to (i) beside the sidewall of buildings and (ii) above the roofs for turbine installation. The specified heights of horizontal x-y planes for the high-level buildings and above the roofs are $z/H=0.93$ and 1.03 , respectively. The vertical x-z planes are selected at a distance of 1.5 m beside the sidewalls and along the middle 3-column of buildings above the roofs. For the sake of brevity, only the wind characteristics for the layouts of compact urban ($\lambda_p = 0.76$), medium urban ($\lambda_p = 0.25$), and sparse urban ($\lambda_p = 0.09$) are presented in Figs. 8-10. The following observations can be made:

- For the regions along the middle of the street canyon of building array in Fig. 8a, the airflows with declining λ_p from 0.76 to 0.09 smoothly permeate through broader street widths into the building array with elevated wind velocities of $V/V_{ref} > 0.9$ (marked in red-color areas) along the passage, caused by the channeling effect between parallel buildings.
- For the regions above the roof in Fig. 8b and 8d, essentially, the approaching wind stagnates and diverges upwardly at the rooftops of first row buildings, and then travels toward the downstream with the decelerating airflows. For the compact urban layout at $\lambda_p = 0.76$, it can be visualized that the shear wind over the roof tends to radiate from the windward corner with the largest expansion angle near the roof. The associated recirculation region above the roof is relatively large with low velocities along the roofs of downstream buildings. In contrast, for the sparse urban layout ($\lambda_p = 0.09$), the recirculation region above the roof is smaller due to the expansion of the high-speed shear wind around the windward corners. We also observe the reattachment of airflows appearing over the roofs of downstream buildings
- For a possible alternative to mount wind turbines at a distance of 1.5 m beside the buildings in Fig. 8c, the maximum wind speed emerges from the corners of 1-row buildings without causing recirculation vortices over the narrowest gap passage for the compact urban layout ($\lambda_p = 0.76$). For the medium urban layout ($\lambda_p = 0.25$), the highest wind speed appears at the leading windward corner, with the sudden deceleration of wind flow resulting from a small recirculating eddy near the wall of 1-row buildings. Taking the sparse urban layout ($\lambda_p = 0.09$) into account, the swirling vortex becomes larger to allow for the development of a relatively high-speed region appearing over 2-row buildings.

Figure 9 presents the predicted contour plots of reference turbulence intensity over the horizontal x-y planes (a) at $z/H = 0.93$ and (b) 1.03 as well as the vertical x-z planes (c) at a distance of 1.5 m beside the buildings and (d) along the middle of building column for the urban layouts of $\lambda_p = 0.76, 0.25, 0.09$.

Here the findings mainly focus on two possible areas for mounting wind turbines as follow:

- For the possible area at a distance of 1.5 m beside the building in Fig. 9a and 9c, the unacceptable I_{ref} regions ($I_{ref} > 0.16$ in orange-red colored areas) for the compact urban layout ($\lambda_p = 0.76$) appear between the 1-row of building array attributable to strongly sheared airflows over the expansion corners. For decreasing λ_p with broader street widths, we view notable extension and separation of the unacceptable I_{ref} regions along the leading-edge windward walls and tend to recur over the wake of each downstream building.
- For an alternative available above the roofs in Fig. 9b and 9d, the wind flows with the compact urban layout ($\lambda_p = 0.76$) are almost completely covered by unfavorable environments with high turbulence intensities. Alternatively, the incoming separation airflows interacting with the sparse urban layout ($\lambda_p = 0.09$) result in the unacceptable I_{ref} region condensed to a height below 1.1 times the building height over the roof corners, allowing for turbine installation at the height above 1.1H.

To investigate the wind energy potential, not only power density but also turbulence level should be taken into account. Hence, we intend to combine these two criteria in this study. Figure 10 shows the contour plots of the normalized power density over the horizontal x-y planes (a) at $z/H = 0.93$ and (b) 1.03 as well as the vertical x-z planes (c) at a distance of 1.5 m beside the buildings and (d) along the middle of building column for $\lambda_p = 0.76, 0.33$ and 0.09 as three scenarios denoting the compact, medium and sparse urban plan area densities, respectively. Note that the high turbulence region of $I_{ref} > 0.16$ is masked in white color, representing its unacceptability for small wind turbine installation base on the IEC standard [59]. Overall, wind power density is directly proportional to the cube of the wind speed. Therefore, the greater the wind speed, the greater the energy potential will be extracted from the wind for conversion to the useful power density through turbine operations.

- For the possible area for harvesting wind energy at a distance of 1.5 m beside the building and $z/H = 0.93$ in Fig. 10a and 10c, the undesirable high turbulence levels (highlighted in white color) appear over the gap passage between and behind those 1st-row buildings for λ_p of 0.76 and 0.33. The acceptable turbulence area with high PD only appears over the gap passage between the back half of 1-row and the front half of 2-row buildings for the compact urban layout ($\lambda_p = 0.76$).
- With the sparse urban layout of $\lambda_p = 0.09$, the unacceptable high turbulence level areas appear over the front half of the windward walls of buildings for every row.
- For the areas above the roofs in Fig. 10b and 10d, the compact urban layout ($\lambda_p = 0.76$) exhibits the most unacceptable high turbulence area extending over the roofs of the nearly whole building array. For the medium urban layout ($\lambda_p = 0.25$), only the roofs of the first 1-, 2-, and 3-row buildings are covered with unsuitably elevated turbulence levels but with lower PD. For the sparse urban layout ($\lambda_p = 0.09$), although the unacceptable I_{ref} regions appear over the roof corners every row, we still view visible high PD areas to install wind turbines.

To sum up, increasing λ_p can reduce both the regions of high wind power density and unacceptable turbulence level for the possible area at a distance of 1.5 m beside the building. Alternately, decreasing λ_p can reduce the region height of unacceptable turbulence areas with relatively higher wind power

density on the roof.

Figure 11 summarizes the predictions of average dimensionless power densities and average reference turbulence intensity of selected areas (i) over the horizontal plane at $z/H= 1.03$ on the roof as well as (ii) the vertical plane at a distance of 1.5 m beside the building for varied urban plan area densities. Those selected areas primarily focus on the prearranged central high-rise buildings as the promising locations for turbine installation, with the area-weighted average wind power densities calculated over the horizontal plane at $z/H= 1.03$ above the roof of 3-row buildings as well as the vertical plane at a distance of 1.5 m beside the 3-row buildings, respectively.

- For the selected areas at a distance of 1.5 m beside the building with the vertical extent of z/H ranging from 0.5 to 1 (in orange-colored lines), the maximum averaged PD/PD_{ref} appears at $\lambda_p= 0.33$. It can be attributed that an optimal layout of urban density is inclined to maximize the power density because of the wind undergoing the channeling effect of the passage between parallel buildings. However, a further decrease in λ_p can reduce the averaged PD/PD_{ref} and increase the averaged I_{ref} . Nevertheless, we still observe the acceptable averaged I_{ref} level with λ_p below the middle urban layout (at $\lambda_p= 0.25$).
- For the selected areas on the roof at $z/H= 1.03$ (in green lines), the averaged PD/PD_{ref} increases by reducing λ_p from the compact to sparse urban layouts, leading to dramatic upsurges of power density at particularly low λ_p values. We also observe the maximum averaged PD/PD_{ref} of 0.32 for the sparse urban layout ($\lambda_p = 0.09$) of 3-row buildings. Besides, a reduction in λ_p can achieve the lowest possible averaged I_{ref} of around 0.16.

4.2. Impact of building corner shape

Generally, building geometry plays a significant role in enhancing the wind power in urban areas. This study implements the rounded corners on only the central 2×2 array of four high-rise buildings to compare the wind power potentials between the sharp and rounded building corner shapes for varied urban plan area densities. Figures 12 and 13 show the predicted contour plots of dimensionless power density (with unacceptable turbulence region highlighted in white color) over the vertical x-z planes (a) at a distance of 1.5 m beside the buildings as well as the horizontal x-y planes (b) at $z/H= 0.5$ and (c) 1.03 for the sharp/round corners and urban densities λ_p of 0.25/0.09, respectively. Overall, the results reveal the significant impact of building corner shape on wind power potential. Detailed observations are provided as below:

- For those selected areas at a distance of 1.5 m beside the building (Fig.12a-b and 13a-b): The predictions having the sharp corner shape present the relatively high PD beside the leading edge of 3-row buildings, with a quick decrease in PD along the gap passage toward the downstream. In contrast, for the round corners, we notice the appearance of high PD regions extending to the windward and leeward round corners of both 3-row and 4-row buildings for $\lambda_p= 0.25$ depicted in Fig.12a-b. For the sparse urban layout ($\lambda_p= 0.09$), the high PD regions even emerge on the leeward

round corners of the roof with no visible unacceptable I_{ref} regions in Fig.13a. This can be attributed to the continuous expansion of airflows over the round corners to produce high wind energy due to accelerated speeds and low-level of turbulence, as compared to those of sharp corners.

- For those selected areas on the roofs at $z/H= 1.03$ (Fig.12c and 13c): It can be seen that a more compact urban layout (λ_p of 0.25) shows a more unacceptable turbulence region than that of $\lambda_p = 0.09$ on the roofs. Considering the scenario of sharp corners for the sparse urban layout ($\lambda_p = 0.09$) in Fig.13c, the wind passes over the roof corners of buildings on the windward side of each row, and induces locally unacceptable turbulence regions around the windward roof corners. Alternatively, the round corner shape can reduce the unacceptable turbulence region due to its aerodynamic corner shape. The power densities on the roofs of 4-row buildings (with the windward buildings using round corners) are substantially higher than those on the roofs of 3-row buildings (with the windward buildings having the sharp corner shape).

It is obvious that the round corner shape can result in a higher PD and a lower I_{ref} over the downstream buildings. In addition, when λ_p increased, the round corner shape produces higher PD outcomes than the sharp corner shape for the installable areas beside the buildings. When λ_p decreased, higher power densities appear over the round corners for the installable areas on the roofs, as compared to the case of sharp corners. These results are consistent with the findings from the impact study of urban density.

To explore the effect of varied upstream building corner shapes on the downstream buildings, we focus on the wind environments around the selected 4-row buildings in the center of the building array. Figures 14 shows the contour plots of dimensionless power density (with the unacceptable I_{ref} region in white color) (a) beside the 4-row buildings over the horizontal x-y planes at $z/H= 0.93$, and (b) on the 4-row roofs along the vertical x-z planes in the middle of 4-row buildings for the sharp/round corners and the urban layouts of $\lambda_p = 0.09, 0.25$, and 0.59 . Detailed observations of close to building corners are provided as below:

- For the selected area beside the buildings at $z/H= 0.93$ (in Fig.14a): By decreasing λ_p from 0.59 to 0.09 for the sharp corners, we noticeably observe the detachment of separating flows from the sharp windward corner with the regions of higher PD and more unacceptable I_{ref} . This event may be attributed to narrow street canyons for high urban densities, causing the breakdown of flow separation from upstream buildings to reattach to the sidewall surfaces of downstream buildings. For the scenario of round corners, we visualize a considerable reduction in the deviation of the shear layer, as compared to the design of sharp λ corners for all urban densities. Decreasing λ_p from 0.59 to 0.09 for the round corner layout is more evident to enhance PD/PD_{ref} from 0.2 to 0.6 around the windward and leeward round corners with increasing unacceptable I_{ref} regions along with the windward round corner. Hence, the region around the leeward round corner near the sidewall can be the suitable mounting locations with high PD and acceptable I_{ref} for wind energy harvesting.
- For the selected area on the roofs along the middle of 4-row buildings (Fig.14b): In the scenario of sharp corners, we observe the appreciable extension and separation of unacceptable I_{ref} regions from the leading sharp roof corners because of localized and intense velocity gradients associated

with sharply sheared flows occurred in the strong single-stage expansion process. However, the I_{ref} results become relatively lower levels with diminished unacceptable I_{ref} areas for the rounded corners owing to their reduced velocity gradients from the associated continuous-stage expansion processes. Similar findings were reported by Toja-Silva et al. [6] to highlight the significance of roof corner modifications in diminishing the unacceptable I_{ref} region, especially on the rooftop. In decreasing λ_p from 0.59 to 0.09, the sharp corners are more exposed to flow separation from the leading sharp roof corners with higher PD and more unacceptable I_{ref} regions. However, round corners of $\lambda_p=0.59$ appear to be ineffective in increasing PD and minimizing the unacceptable I_{ref} area. The round corners of $\lambda_p = 0.25$ start to decrease the extent of separated shear layer flows around the leading round corner with slightly increasing PD/PD_{ref} up to 0.3. When coming to $\lambda_p=0.09$, the case of round corners shows a significant increase in PD/PD_{ref} up to 0.6 and contracting the unacceptable I_{ref} region around the windward roof.

Figure 15 shows the predicted profiles of wind power density and reference turbulence intensity along the building length of two selected areas (a) beside the building and (b) on the roof for the sharp/round corners at varied urban densities. By comparing all the simulation results between sharp and round corner shapes at different urban densities, here the selected area beside the building has a prescribed distance of 1.5 m beside the sidewall of 4-row buildings at the height of $z/H=0.93$, while the selected area on the roof highlights the middle of the roof of 4-row buildings at the height of $z/H=1.03$. We can carefully examine the PD and I_{ref} profiles against building length at the considering mounting sites for resolving the best installation locations. The observations are summed as below:

- For the selected line beside the building (Fig.15a): The case with the round corners for $\lambda_p = 0.09$ shows the highest PD/PD_{ref} near the leeward round corners. The maximum values of PD/PD_{ref} for the round corner shape are 201%, 55%, 36%, 4% and 12% higher than those of sharp corners for $\lambda_p = 0.09, 0.25, 0.33, 0.48, \text{ and } 0.59$, respectively. Only for $\lambda_p = 0.79$, the maximum PD/PD_{ref} value for the round corner is 11% lower than that of the sharp corner. From the I_{ref} profiles at $\lambda_p=0.09$, the round corner shape attains the acceptable turbulence level, while the wind environments with the sharp corners exceed the maximum allowable 0.16. For other urban densities of $\lambda_p \geq 0.25$, I_{ref} values of the round corner are slightly higher than those of the sharp corner; nevertheless, the I_{ref} results are in the satisfactory range. In addition, I_{ref} profiles for $\lambda_p \geq 0.25$ are primarily reduced with higher λ_p settings.
- For the selected line on the roofs (Fig.15b): The case with the round corner for $\lambda_p = 0.09$ has the highest PD/PD_{ref} near the windward and leeward round corners. The maximum PD/PD_{ref} values for round corners are 150% and 5% greater than those of sharp corners along the whole line for $\lambda_p = 0.09$ and 0.25, respectively. For these cases, we observe suitable I_{ref} values (≤ 0.16) over the region for the round corner of $\lambda_p = 0.09$ and 0.25. Conversely, the maximum PD/PD_{ref} values for the round corner shape are lower than those of sharp corner by 16%, 11%, 44% and 1% for $\lambda_p = 0.33, 0.48, 0.59, \text{ and } 0.79$, respectively.

4.3. Impact of urban layout

In this impact, two urban densities of 0.5 and 0.25 are considered, with high-rise buildings in the staggered pattern. Figure 16 shows the predicted contour plots of (a) dimensionless velocity magnitude and (b) dimensionless power density (with unacceptable turbulence region marked in white color) over the horizontal x-y plane at $z/H= 0.93$ for the sharp/round corners and staggered urban layouts. Here the wind power results with the staggered urban layout are used to compare with those of the in-line urban layout. The predictions reveal that the staggered urban layout tends to decrease the air velocities with relatively low wind power densities produced because of higher flow resistance, as compared to the scenario of the in-line urban layout. As depicted in Fig.16a, the infiltration wind speeds in the 2-row to 4-row for $\lambda_p = 0.25$ are higher than those for $\lambda_p = 0.5$ because of its reduced urban density and lower overlapping windward surface ratio, indicating a poorer ventilation efficiency for the staggered urban layout. Overall, the obstruction effect in the staggered high-rise buildings array can produce more significant areas of low power densities and high turbulence intensities than those of the in-line urban layout, as shown in Fig.16b. First-row high-rise buildings involve more than half windward surfaces in 2-row of buildings, revealing impinging airflows with high turbulence intensities appeared in the first three rows.

4.4. Impact of wind direction

Figure 17 shows the predicted contour plots of dimensionless power density (with unacceptable turbulence region marked in white color) over the horizontal planes at $z/H= 0.93$ and 1.03 with the oblique wind direction θ of 45° for different building corner shapes. As compared to the wind direction of 0° for the sharp corner shape in Fig. 10ab, we notice more unacceptable turbulence areas and less high PD/PD_{ref} regions at the heights of $z/H= 0.93$ and 1.03 with $\theta= 45^\circ$ for all urban densities. Besides, declining λ_p can increase the unacceptable turbulence areas for both sharp and round corners at z/H of 0.93 in Fig.17a. For the rounded corner layout at $z/H= 1.03$ at $\lambda_p= 0.76$ in Fig.17b, excellent PD/PD_{ref} outcomes up to 0.6 with appropriate I_{ref} appear over the roof of the center 2×2 building array, with the power densities much greater than those of the sharp corner layout. For $\lambda_p= 0.09$, round corners also achieve a higher PD/PD_{ref} up to 0.38 than the sharp corners. Thus, round corners still have better wind power densities than those of sharp corners with an oblique wind direction of 45° .

5. Discussion

The limitations of this study are illustrated as follows:

- (1) This study considers the scenario of an array of uniform-height high-rise buildings as the most generic urban morphology. The impacts of non-uniform building height or unequal building arrangements (i.e., unequal street canyon widths) on wind energy harvesting are not yet taken into account.
- (2) This study primarily performs the analyses using the regular cuboid of high-rise buildings.

The aspect ratios of cuboids will be varied to better select the most suitable building corner modifications in further investigations.

- (3) Steady-state CFD simulations are conducted at a fixed wind direction. Any possible airflow unsteadiness and variations in the intermittency and variability of wind speed and direction are not considered in detail.
- (4) Other determinants are strongly bearing on the urban wind environments, such as air quality, air pollutant dispersion, wind energy potential, heat island effect, which can be thoroughly examined for sustainable urban development.

6. Conclusions

The parametric studies to inclusively evaluate various impacts of urban morphology on the wind power potential and turbulence intensity around high-rise building arrays have been examined through the CFD simulations. These impacts are: (i) urban density, (ii) building corner shape, (iii) urban layout, and (iv) wind direction. This study has revealed the effectiveness of apposite modifications of urban morphology for high-rise building array to significantly enhance wind power densities with reduced turbulence intensities over the two viable areas for turbine installation: (I) beside the sidewall and (II) above the roof of buildings, which can be summarized as follows:

- Decreasing λ_p can diminish the unacceptable turbulence areas with relatively higher wind power densities on the installable areas above the roofs.
- On the installable areas beside the buildings, it is noted that the maximum average PD with the acceptable average I_{ref} occurs at $\lambda_p=0.33$, suggesting the significance of the most favorable urban density to accelerate local wind speeds and wind power density.
- The continuous expansion of airflows over the round corner shape can produce high wind power densities and low turbulence intensities around the downstream buildings, as compared to those of sharp corners.
- Round corners for $\lambda_p=0.09$ show the highest PD/PD_{ref} results up to 201% and 150% than those of sharp corners for two selected areas beside the building and on the roof, respectively.
- The in-line urban layout can realize more significant areas of elevated power densities and low turbulence intensities than those of the staggered urban layout.
- An oblique wind direction of 45° produces more unacceptable turbulence level areas and less high power density regions for all urban densities, as compared to the wind direction of 0° .
- Even under the oblique wind direction of 45° , the rounded corners still have more areas of high wind power potentials with acceptable I_{ref} over the rooftop, as compared to the sharp corner case.

Acknowledgment

This study represents part of the results obtained under the support of the Ministry of Science and Technology, Taiwan, ROC (Contract No. MOST108-2221-E-027-041 and 107-2917-I-027-001).

Nomenclature

ABL	= Atmospheric boundary layer
B	= Building length
CFD	= Computational fluid dynamics
C_s	= Roughness constant
ε	= Turbulent dissipation rate
H	= Building height
H/W	= Building-height-to-street-width ratio
I_{ref}	= Reference turbulence intensity
k	= Turbulent kinetic energy
k_s	= Sand-grain roughness height
PD	= Power density
PD_{ref}	= Reference power density
RANS	= Reynolds-averaged Navier-Stokes
RSM	= Reynolds stress model
TI	= Turbulence intensity
TI	= Incident vertical profiles of turbulence intensity
TI_{ref}	= Reference turbulence intensity at reference height H
u	= Streamwise mean velocity component
u	= Incident vertical profiles of streamwise mean velocity component
$U(z)_{ABL}$	= Mean inlet velocity of atmospheric boundary layer
u_{ABL}^*	= ABL friction velocity
U_{ref}	= Reference wind speed
u_{ref}	= Reference streamwise mean velocity component
v	= Cross-stream velocity
V	= Velocity magnitude
V_{ref}	= Reference velocity magnitude
w	= Spanwise velocity
W	= Gap width between buildings
x, y, z	= Coordinates
y^*	= y plus
z_0	= Aerodynamic roughness length
κ	= von Karman's constant, 0.42
ρ	= Air density

Reference

- [1] Kc A, Whale J, Urmee T. Urban wind conditions and small wind turbines in the built environment: A review. *Renewable Energy*. 2019;131:268-83.
- [2] Rezaeiha A, Montazeri H, Blocken B. A framework for preliminary large-scale urban wind energy potential assessment: Roof-mounted wind turbines. *Energy Conversion and Management*. 2020;214:112770.
- [3] Stathopoulos T, Alrawashdeh H, Al-Quraan A, Blocken B, Dilimulati A, Paraschivoiu M, et al. Urban wind energy: Some views on potential and challenges. *Journal of Wind Engineering and Industrial Aerodynamics*. 2018;179:146-57.
- [4] Bibri SE, Krogstie J, Kärrholm M. Compact city planning and development: Emerging practices and strategies for achieving the goals of sustainability. *Developments in the Built Environment*. 2020;4:100021.
- [5] Toja-Silva F, Kono T, Peralta C, Lopez-Garcia O, Chen J. A review of computational fluid dynamics (CFD) simulations of the wind flow around buildings for urban wind energy exploitation. *Journal of Wind Engineering and Industrial Aerodynamics*. 2018;180:66-87.
- [6] Toja-Silva F, Lopez-Garcia O, Peralta C, Navarro J, Cruz I. An empirical–heuristic optimization of the building-roof geometry for urban wind energy exploitation on high-rise buildings. *Applied Energy*. 2016;164:769-94.
- [7] Hassanli S, Hu G, Kwok KCS, Fletcher DF. Utilizing cavity flow within double skin façade for wind energy harvesting in buildings. *Journal of Wind Engineering and Industrial Aerodynamics*. 2017;167:114-27.
- [8] Larin P, Paraschivoiu M, Aygun C. CFD based synergistic analysis of wind turbines for roof mounted integration. *Journal of Wind Engineering and Industrial Aerodynamics*. 2016;156:1-13.
- [9] Kono T, Kogaki T, Kiwata T. Numerical Investigation of Wind Conditions for Roof-Mounted Wind Turbines: Effects of Wind Direction and Horizontal Aspect Ratio of a High-Rise Cuboid Building. *Energies*. 2016;9:907.
- [10] Juan YH, Wen CY, Chen WY, Yang AS. Numerical assessments of wind power potential and installation arrangements in realistic highly urbanized areas. *Renewable and Sustainable Energy Reviews*. 2021;135:110165.
- [11] Juan Y-H, Yang A-S, Wen C-Y, Lee Y-T, Wang P-C. Optimization procedures for enhancement of city breathability using arcade design in a realistic high-rise urban area. *Building and Environment*. 2017;121:247-61.
- [12] Yang A-S, Su Y-M, Wen C-Y, Juan Y-H, Wang W-S, Cheng C-H. Estimation of wind power generation in dense urban area. *Applied Energy*. 2016;171:213-30.
- [13] Tong Z, Chen Y, Malkawi A. Defining the Influence Region in neighborhood-scale CFD simulations for natural ventilation design. *Applied Energy*. 2016;182:625-33.
- [14] Chow WK. Wind-induced indoor-air flow in a high-rise building adjacent to a vertical

wall. *Applied Energy*. 2004;77:225-34.

[15] Chen L, Hang J, Sandberg M, Claesson L, Di Sabatino S, Wigo H. The impacts of building height variations and building packing densities on flow adjustment and city breathability in idealized urban models. *Building and Environment*. 2017;118:344-61.

[16] Ramponi R, Blocken B, de Coo LB, Janssen WD. CFD simulation of outdoor ventilation of generic urban configurations with different urban densities and equal and unequal street widths. *Building and Environment*. 2015;92:152-66.

[17] Hang J, Li Y, Sandberg M, Buccolieri R, Di Sabatino S. The influence of building height variability on pollutant dispersion and pedestrian ventilation in idealized high-rise urban areas. *Building and Environment*. 2012;56:346-60.

[18] Wang W, Wang X, Ng E. The coupled effect of mechanical and thermal conditions on pedestrian-level ventilation in high-rise urban scenarios. *Building and Environment*. 2021;191:107586.

[19] Cui D, Hu G, Ai Z, Du Y, Mak CM, Kwok K. Particle image velocimetry measurement and CFD simulation of pedestrian level wind environment around U-type street canyon. *Building and Environment*. 2019;154:239-51.

[20] Chen L, Mak CM. Numerical evaluation of pedestrian-level wind comfort around “lift-up” buildings with various unconventional configurations. *Building and Environment*. 2021;188:107429.

[21] Nasir DSNM, Hughes BR, Calautit JK. A CFD analysis of several design parameters of a road pavement solar collector (RPSC) for urban application. *Applied Energy*. 2017;186:436-49.

[22] Nazarian N, Kleissl J. CFD simulation of an idealized urban environment: Thermal effects of geometrical characteristics and surface materials. *Urban Climate*. 2015;12:141-59.

[23] Chen Y, Hong T. Impacts of building geometry modeling methods on the simulation results of urban building energy models. *Applied Energy*. 2018;215:717-35.

[24] Perera ATD, Javanroodi K, Nik VM. Climate resilient interconnected infrastructure: Co-optimization of energy systems and urban morphology. *Applied Energy*. 2021;285:116430.

[25] Peng LLH, Jiang Z, Yang X, Wang Q, He Y, Chen SS. Energy savings of block-scale facade greening for different urban forms. *Applied Energy*. 2020;279:115844.

[26] Hassan AM, Elmokadem AA, Megahed NA, Abo Eleinen OM. Urban morphology as a passive strategy in promoting outdoor air quality. *Journal of Building Engineering*. 2020;29:101204.

[27] Hang J, Wang Q, Chen X, Sandberg M, Zhu W, Buccolieri R, et al. City breathability in medium density urban-like geometries evaluated through the pollutant transport rate and the net escape velocity. *Building and Environment*. 2015;94:166-82.

[28] Hang J, Li Y. Age of air and air exchange efficiency in high-rise urban areas and its link to pollutant dilution. *Atmospheric Environment*. 2011;45:5572-85.

- [29] Buccolieri R, Sandberg M, Di Sabatino S. City breathability and its link to pollutant concentration distribution within urban-like geometries. *Atmospheric Environment*. 2010;44:1894-903.
- [30] Javanroodi K, Mahdavinejad M, Nik VM. Impacts of urban morphology on reducing cooling load and increasing ventilation potential in hot-arid climate. *Applied Energy*. 2018;231:714-46.
- [31] Montazeri H, Blocken B. CFD simulation of wind-induced pressure coefficients on buildings with and without balconies: Validation and sensitivity analysis. *Building and Environment*. 2013;60:137-49.
- [32] Balduzzi F, Bianchini A, Carnevale EA, Ferrari L, Magnani S. Feasibility analysis of a Darrieus vertical-axis wind turbine installation in the rooftop of a building. *Applied Energy*. 2012;97:921-9.
- [33] Walker SL. Building mounted wind turbines and their suitability for the urban scale—A review of methods of estimating urban wind resource. *Energy and Buildings*. 2011;43:1852-62.
- [34] Toja-Silva F, Colmenar-Santos A, Castro-Gil M. Urban wind energy exploitation systems: Behaviour under multidirectional flow conditions—Opportunities and challenges. *Renewable and Sustainable Energy Reviews*. 2013;24:364-78.
- [35] Li QS, Shu ZR, Chen FB. Performance assessment of tall building-integrated wind turbines for power generation. *Applied Energy*. 2016;165:777-88.
- [36] Ge M, Zhang S, Meng H, Ma H. Study on interaction between the wind-turbine wake and the urban district model by large eddy simulation. *Renewable Energy*. 2020;157:941-50.
- [37] Wang Q, Wang J, Hou Y, Yuan R, Luo K, Fan J. Micrositing of roof mounting wind turbine in urban environment: CFD simulations and lidar measurements. *Renewable Energy*. 2018;115:1118-33.
- [38] Wang B, Cot LD, Adolphe L, Geoffroy S. Estimation of wind energy of a building with canopy roof. *Sustainable Cities and Society*. 2017;35:402-16.
- [39] Kono T, Kogaki T. Numerical Investigation of Wind Conditions over a Rectangular Prism-Shaped Building for Mounting Small Wind Turbines. *Wind Engineering*. 2012;36:111-21.
- [40] Zhou H, Lu Y, Liu X, Chang R, Wang B. Harvesting wind energy in low-rise residential buildings: Design and optimization of building forms. *Journal of Cleaner Production*. 2017;167:306-16.
- [41] Heo YG, Choi NJ, Choi KH, Ji HS, Kim KC. CFD study on aerodynamic power output of a 110 kW building augmented wind turbine. *Energy and Buildings*. 2016;129:162-73.
- [42] Ledo L, Kosasih PB, Cooper P. Roof mounting site analysis for micro-wind turbines. *Renewable Energy*. 2011;36:1379-91.
- [43] Millward-Hopkins JT, Tomlin AS, Ma L, Ingham D, Pourkashanian M. The predictability of above roof wind resource in the urban roughness sublayer. *Wind Energy*. 2012;15:225-43.
- [44] Lu L, Ip KY. Investigation on the feasibility and enhancement methods of wind power

utilization in high-rise buildings of Hong Kong. *Renewable and Sustainable Energy Reviews*. 2009;13:450-61.

[45] Wang B, Cot LD, Adolphe L, Geoffroy S, Morchain J. Estimation of wind energy over roof of two perpendicular buildings. *Energy and Buildings*. 2015;88:57-67.

[46] Balduzzi F, Bianchini A, Ferrari L. Microeolic turbines in the built environment: Influence of the installation site on the potential energy yield. *Renewable Energy*. 2012;45:163-74.

[47] Heath MA, Walshe JD, Watson SJ. Estimating the potential yield of small building-mounted wind turbines. *WIND ENERGY*. 2007;10:271-87.

[48] Abohela I, Hamza N, Dudek S. Effect of roof shape, wind direction, building height and urban configuration on the energy yield and positioning of roof mounted wind turbines. *Renewable Energy*. 2013;50:1106-18.

[49] TFI. Turbulent Flow Instrumentation Cobra Probe. 2020.

[50] Franke J, Baklanov A. Best practice guideline for the CFD simulation of flows in the urban environment COST action 732 Quality assurance and improvement of microscale meteorological models. Hamburg: Meteorological Inst.; 2007.

[51] Casey M, Wintergerste T. ERCOFTAC best practice guidelines : ERCOFTAC special interest group on "quality and trust in industrial CFD". London: ERCOFTAC; 2000.

[52] Jones WP, Launder BE. The prediction of laminarization with a two-equation model of turbulence. *International Journal of Heat and Mass Transfer*. 1972;15:301-14.

[53] Shih T-H, Liou WW, Shabbir A, Yang Z, Zhu J. A new $k-\epsilon$ eddy viscosity model for high Reynolds number turbulent flows. *Computers & Fluids*. 1995;24:227-38.

[54] Yakhot V, Orszag SA, Thangam S, Gatski TB, Speziale CG. Development of turbulence models for shear flows by a double expansion technique. *Physics of Fluids A*. 1992;4:1510-20.

[55] Menter F. Zonal Two Equation $k-\omega$ Turbulence Models For Aerodynamic Flows. 23rd Fluid Dynamics, Plasmadynamics, and Lasers Conference: American Institute of Aeronautics and Astronautics; 1993.

[56] Launder BE, Reece GJ, Rodi W. Progress in the development of a Reynolds-stress turbulence closure. *Journal of Fluid Mechanics*. 1975;68:537-66.

[57] Oke TR. Street design and urban canopy layer climate. *Energy and Buildings*. 1988;11:103-13.

[58] Tominaga Y, Mochida A, Yoshie R, Kataoka H, Nozu T, Yoshikawa M, et al. AIJ guidelines for practical applications of CFD to pedestrian wind environment around buildings. *Journal of Wind Engineering and Industrial Aerodynamics*. 2008;96:1749-61.

[59] I.E.C. International Electrotechnical Commission (IEC) 61400-1 Wind turbines –Part 1: Design requirements 2005.



Figure 1 Photos of high-rise buildings in close proximity in the Kowloon City District, Hong Kong
(photographed by Po-Ki Li).

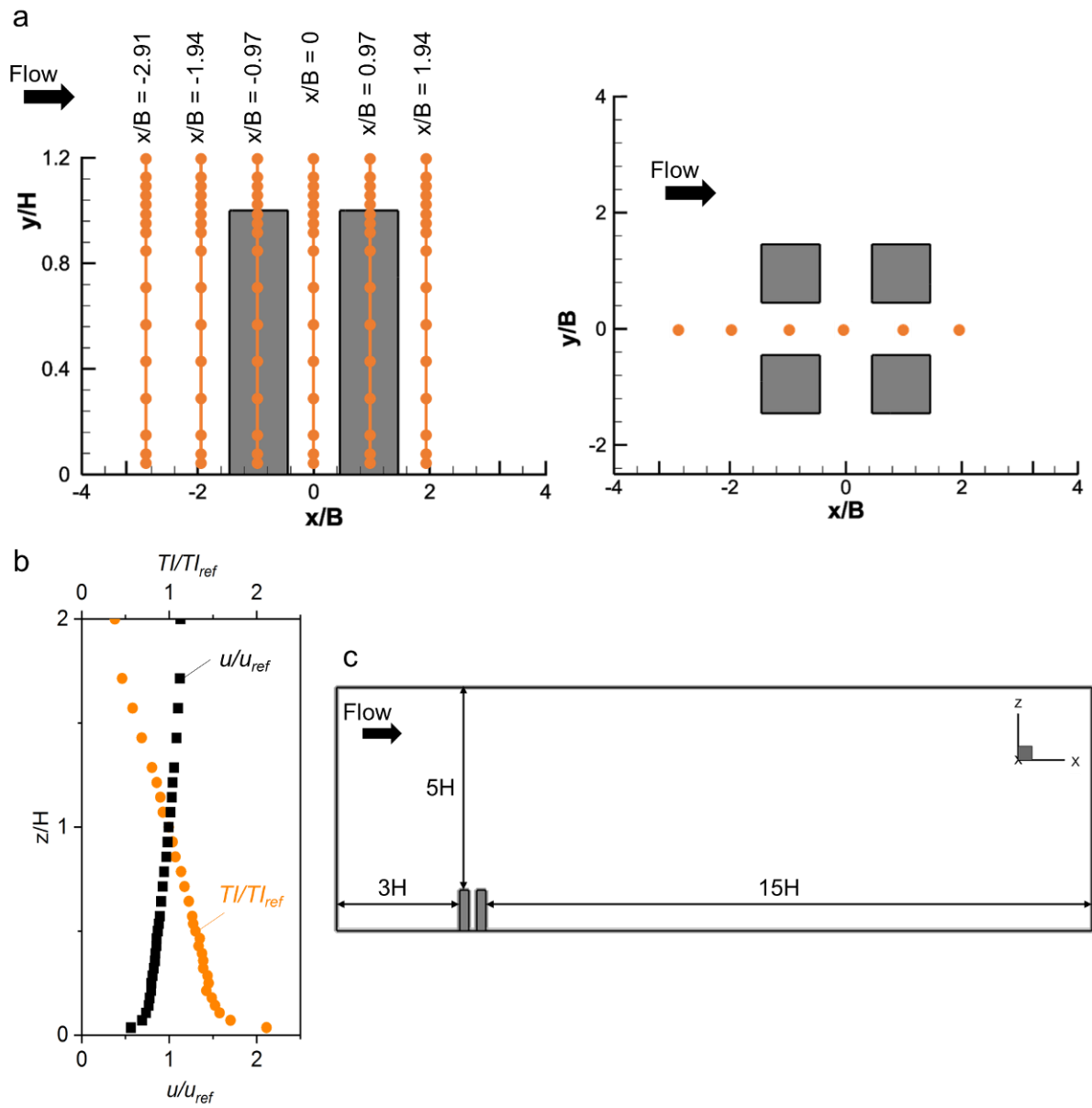


Figure 2 (a) Locations of monitoring points on lateral view of 6 profiles along the vertical centerlines ($y/B = 0$) at 6 positions ($x/B = -2.9, -1.94, -0.97, 0, 0.97$ and 1.94); (b) the dimensionless incident profiles; and (c) the computational domain for CFD validation.

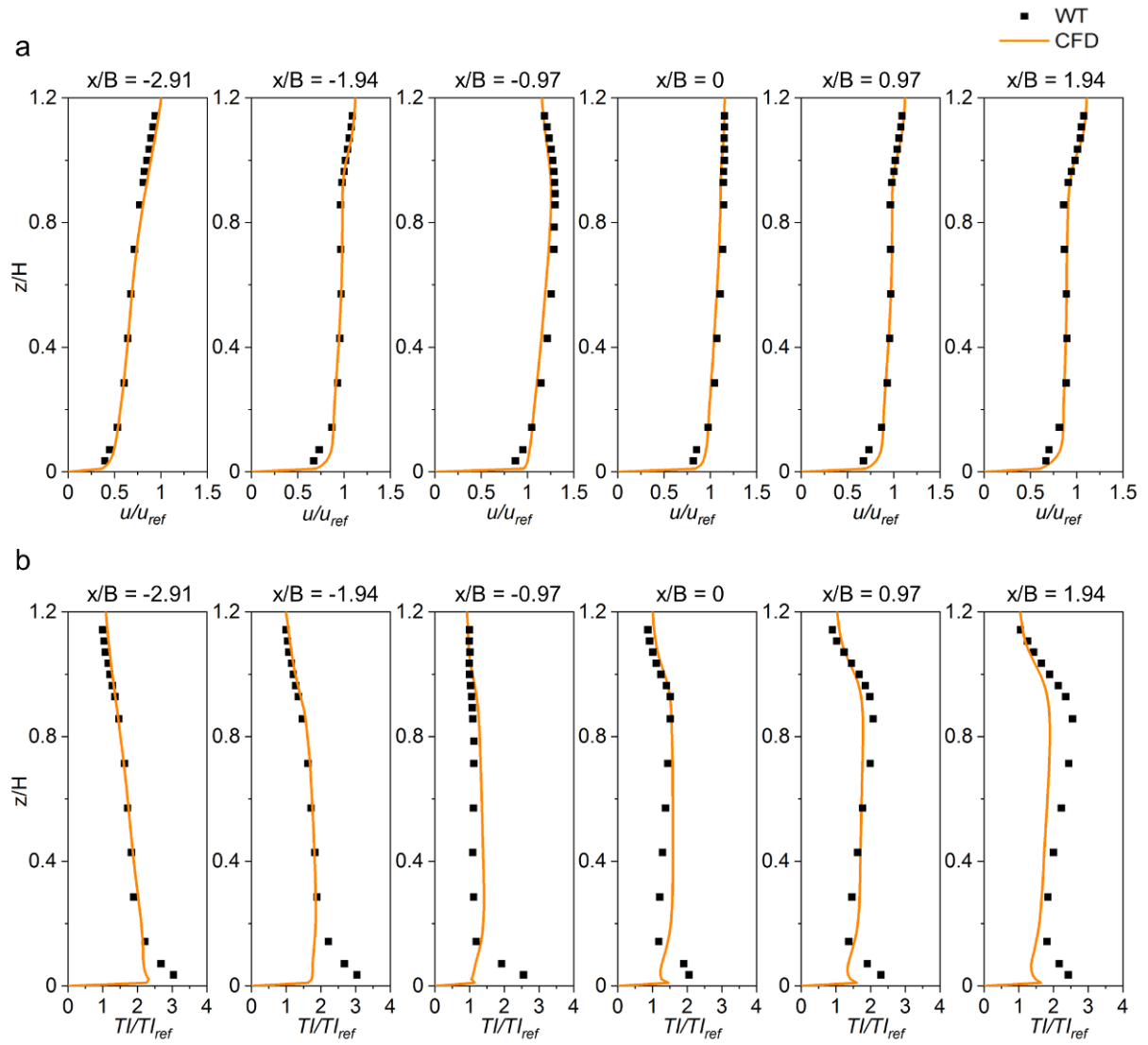


Figure 3 Comparison of (a) time-averaged streamwise velocity component and (b) total turbulence intensity with wind-tunnel measured data along vertical lines at $x/B = -2.9, -1.94, -0.97, 0, 0.97$ and 1.94 .

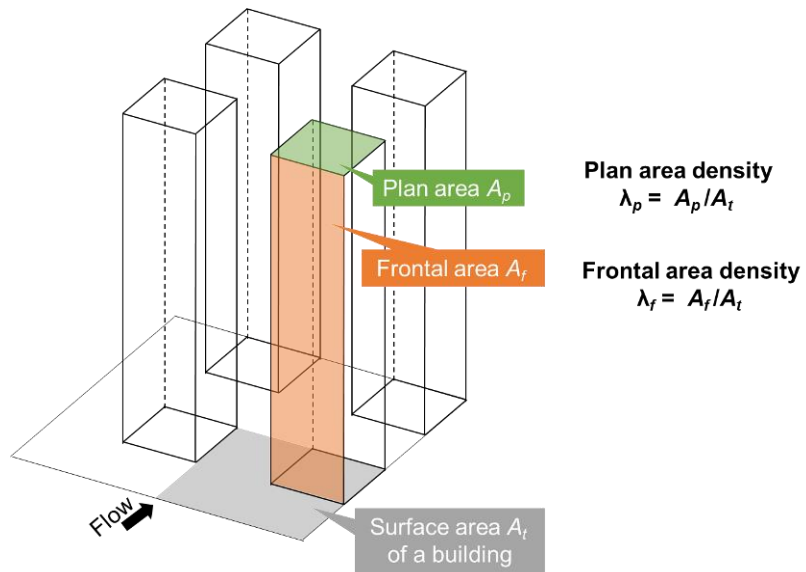


Figure 4 Description of urban plan area density (λ_p) and frontal area density (λ_f).

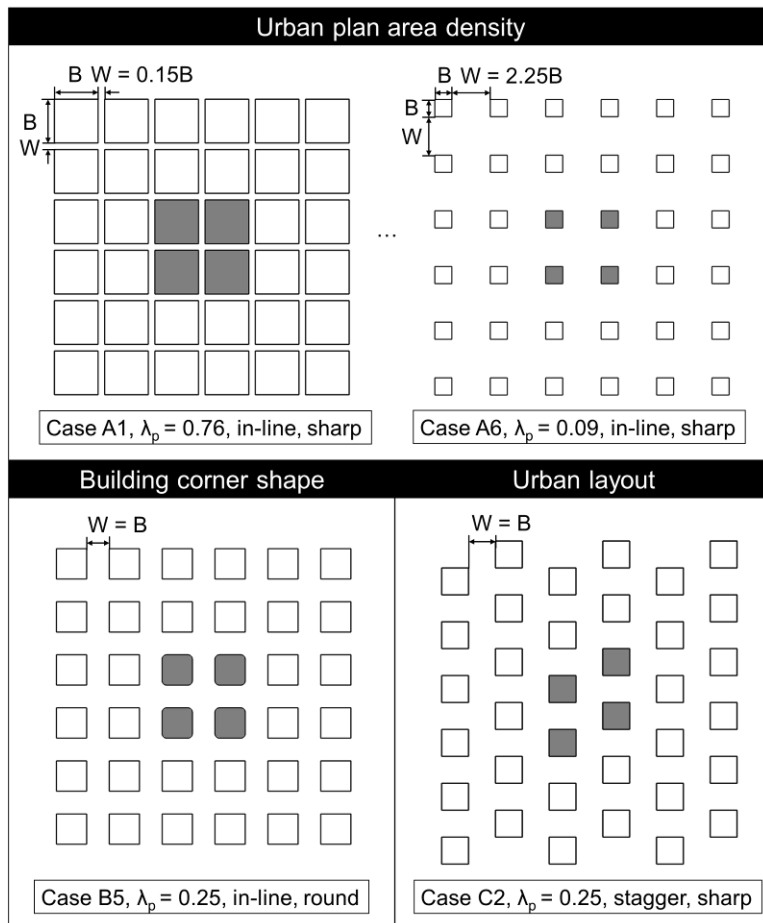


Figure 5 Urban morphologies for different involved parameters.

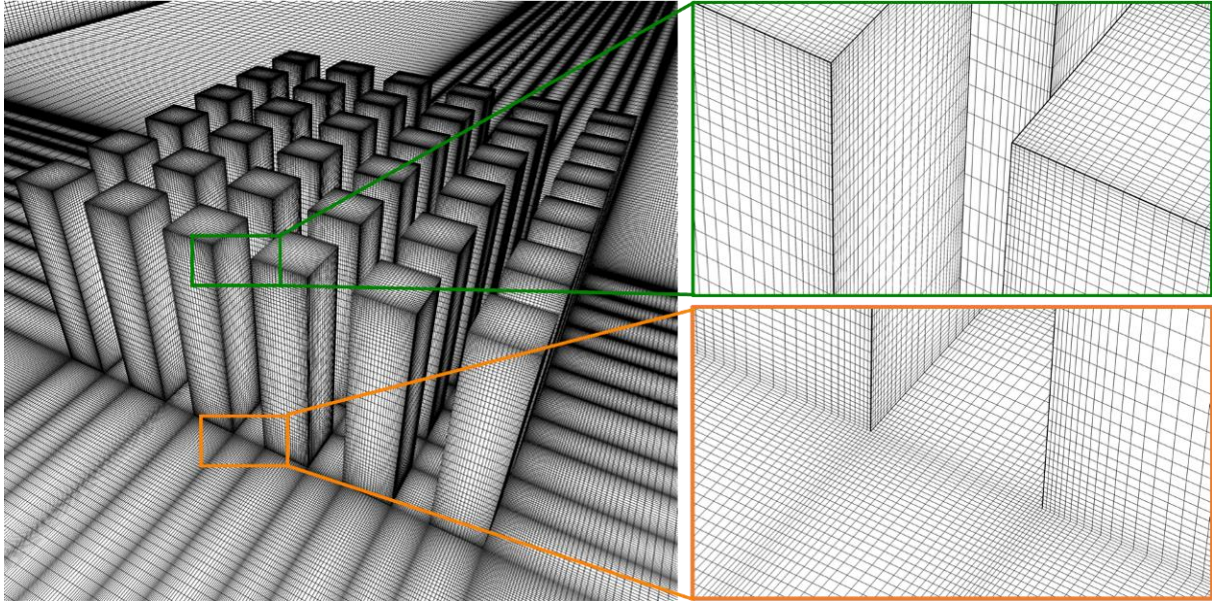


Figure 6 Computational mesh of Case A4 for the base grids, with magnification of grids near roof and ground.

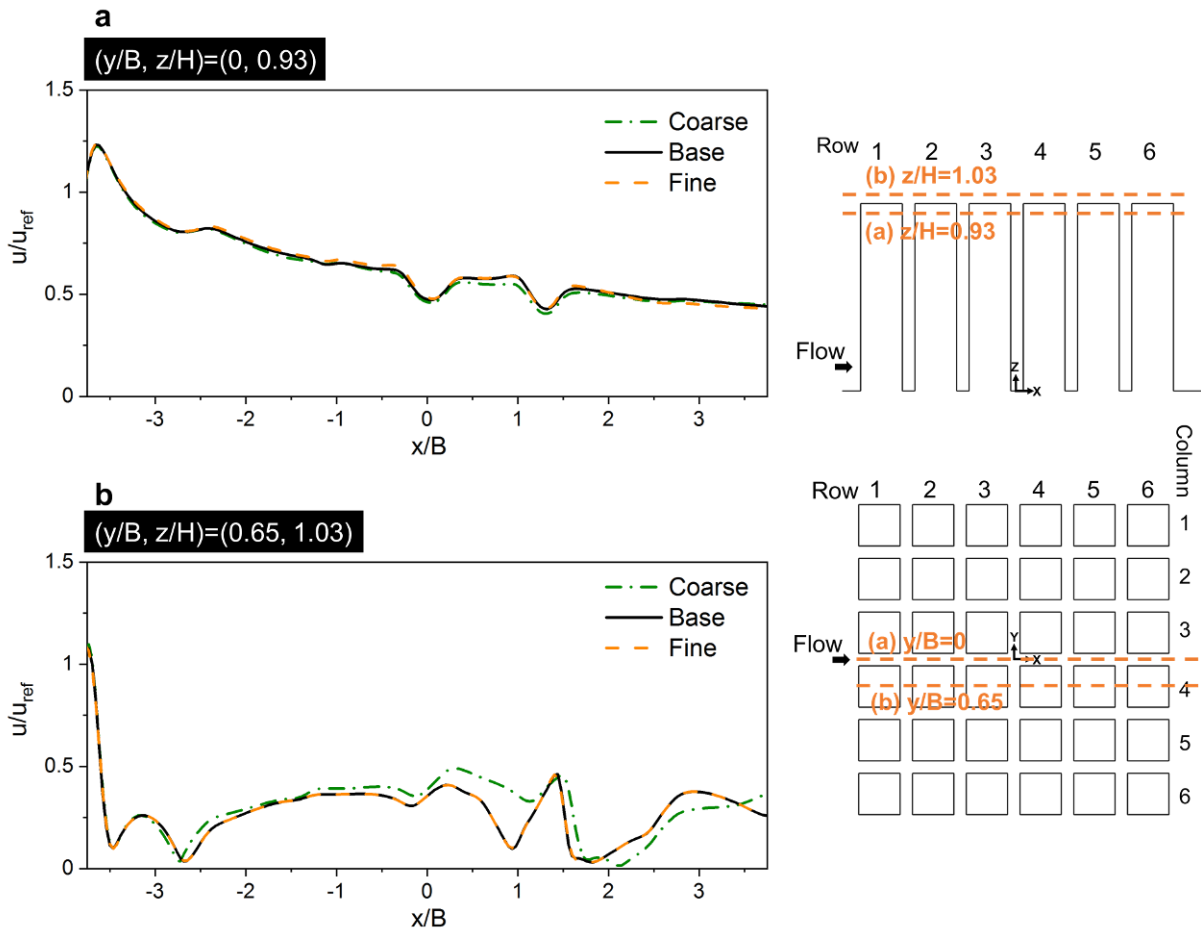


Figure 7 Grid-sensitivity analysis: the dimensionless streamwise velocity component along the centerline of building array at $z/H = 0.93$ for the coarse, base, and fine grids of Case A2.

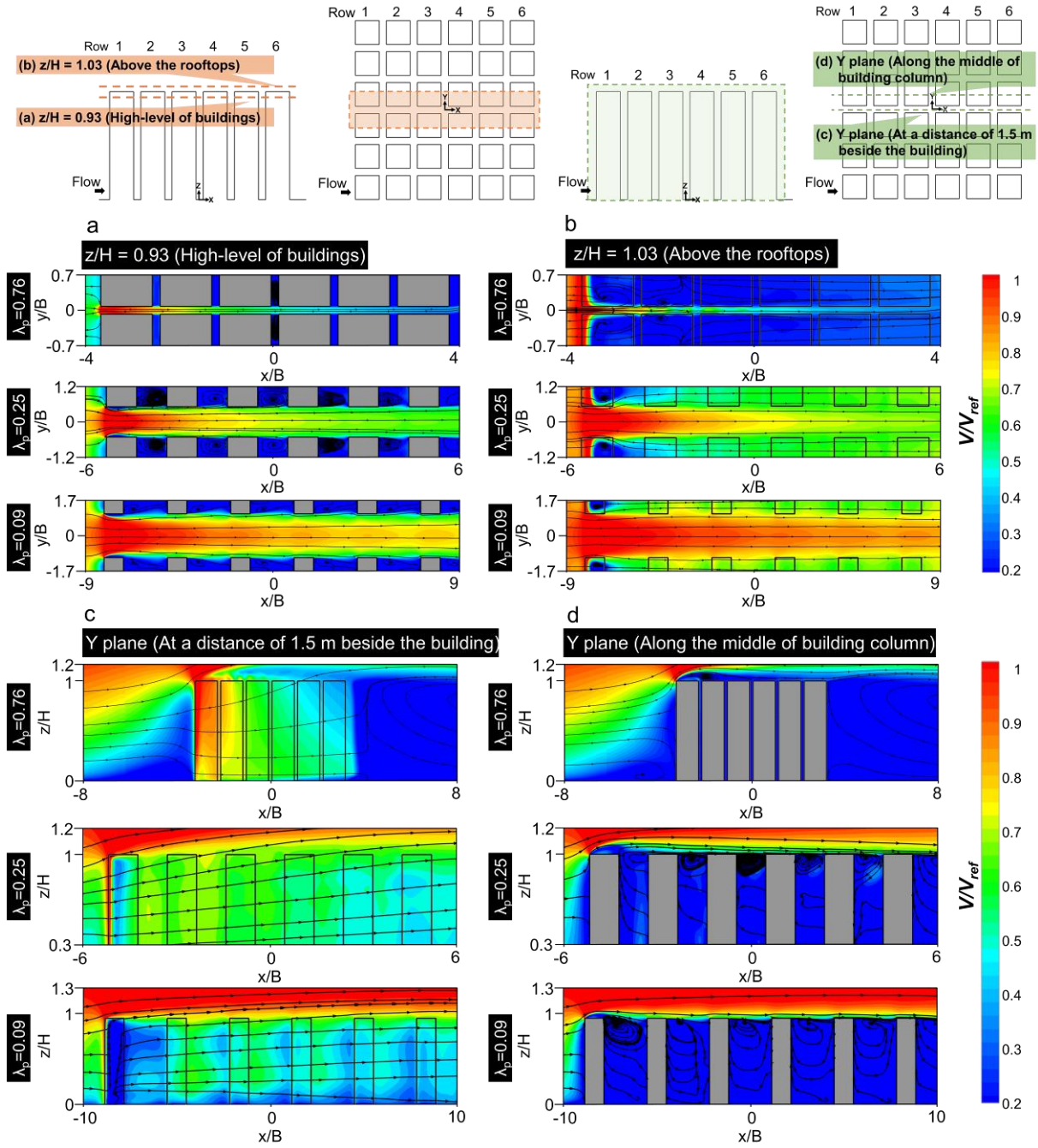


Figure 8 Predicted contour plots of dimensionless velocity magnitude V/V_{ref} (with superimposed streamlines) over the horizontal x-y planes (a) at $z/H= 0.93$ and (b) 1.03 as well as the vertical x-z planes (c) at a distance of 1.5 m beside the buildings and (d) along the middle of building column above the roofs for $\lambda_p = 0.76, 0.25, 0.09$ and the normal wind direction of 0° .

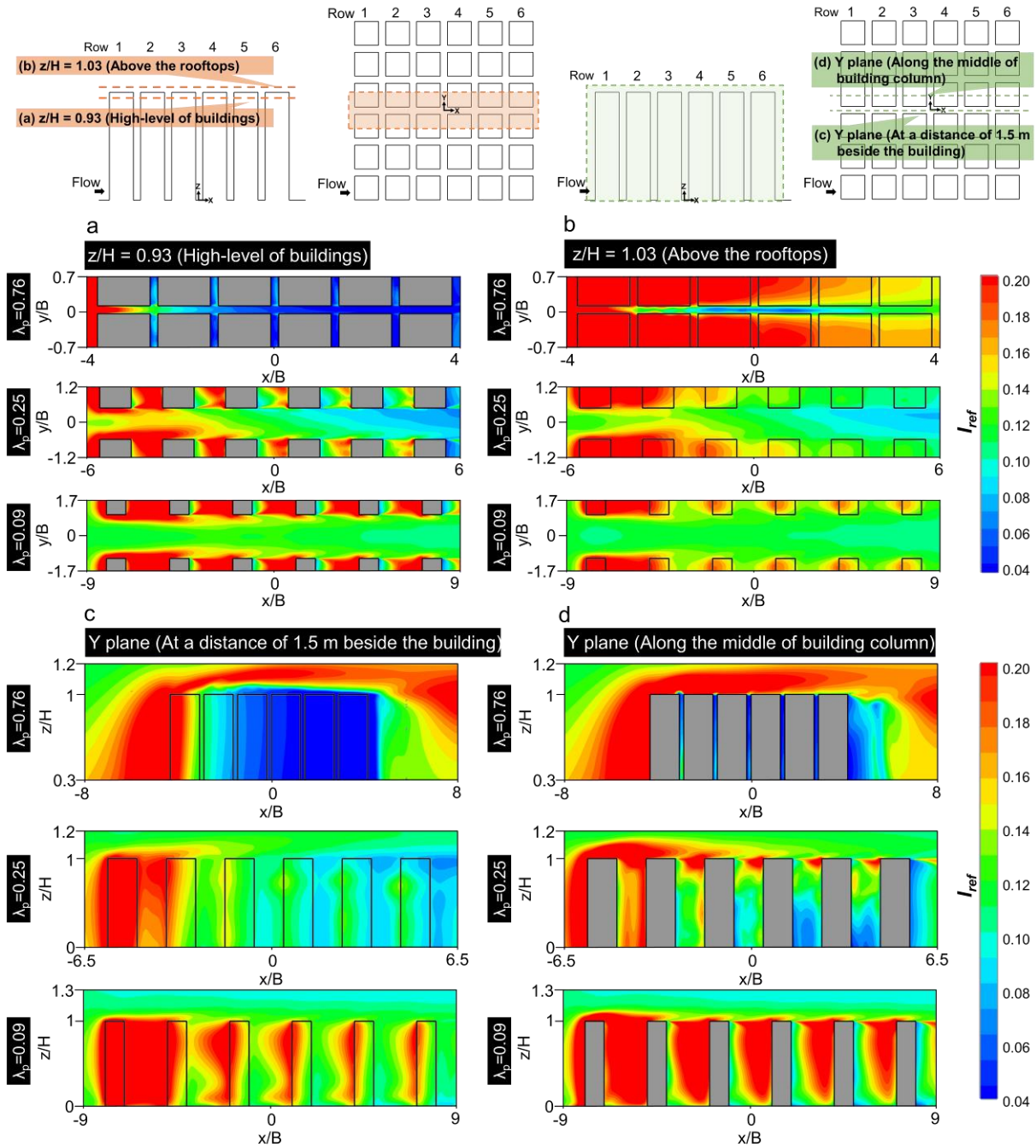


Figure 9 Predicted contour plots of reference turbulence intensity over the horizontal x - y planes (a) at $z/H=0.93$ and (b) 1.03 as well as the vertical x - z planes (c) at a distance of 1.5 m beside the buildings and (d) along the middle of building column for the urban layouts of $\lambda_p=0.76, 0.25, 0.09$ and the normal wind direction of 0° .

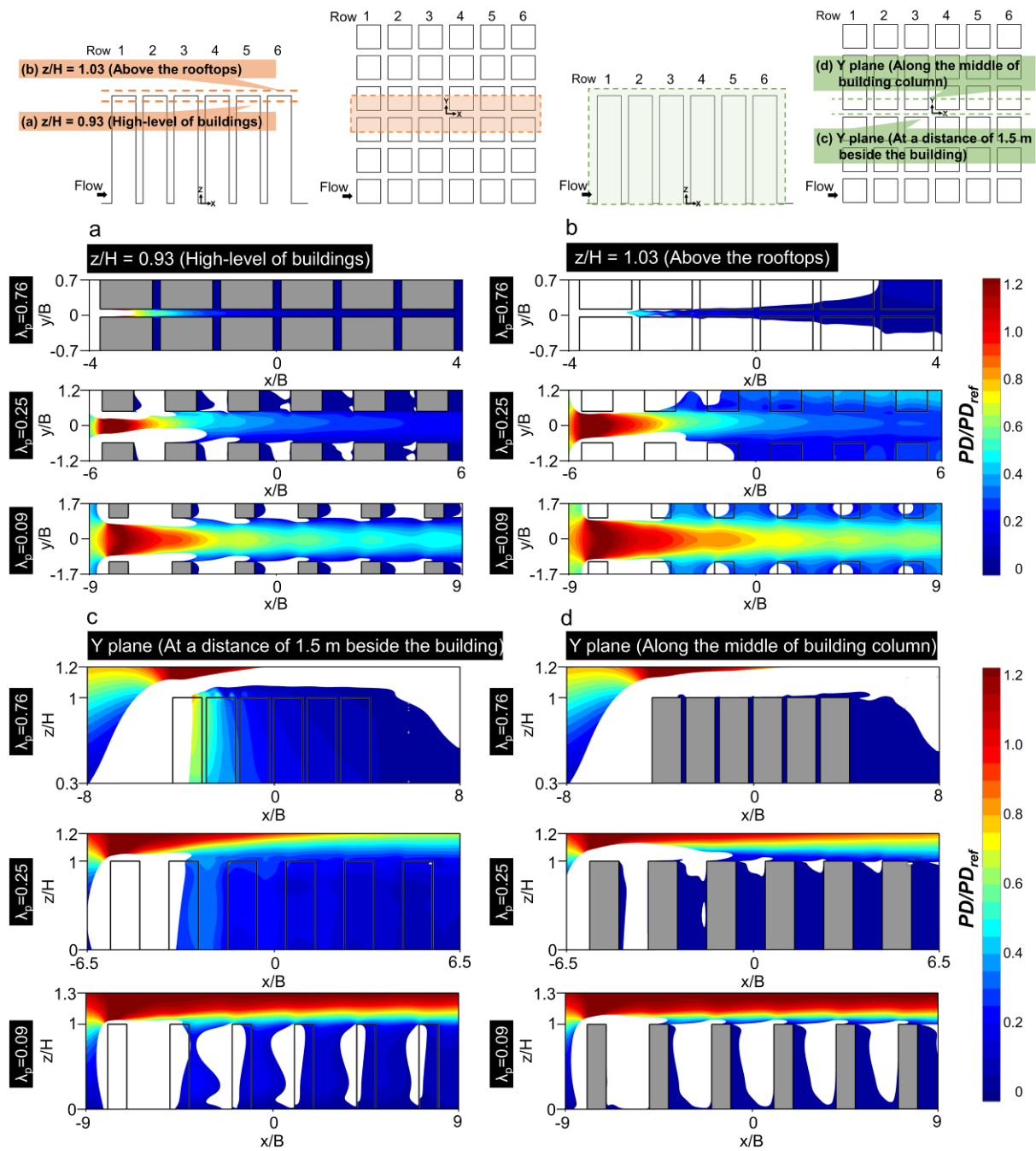


Figure 10 Predicted contour plots of dimensionless power density (with unacceptable turbulence region in white color) over the horizontal x - y planes (a) at $z/H = 0.93$ and (b) 1.03 as well as the vertical x - z planes (c) at a distance of 1.5 m beside the buildings and (d) along the middle of building column for the urban layouts of $\lambda_p = 0.76, 0.25, 0.09$ and the normal wind direction of 0° .

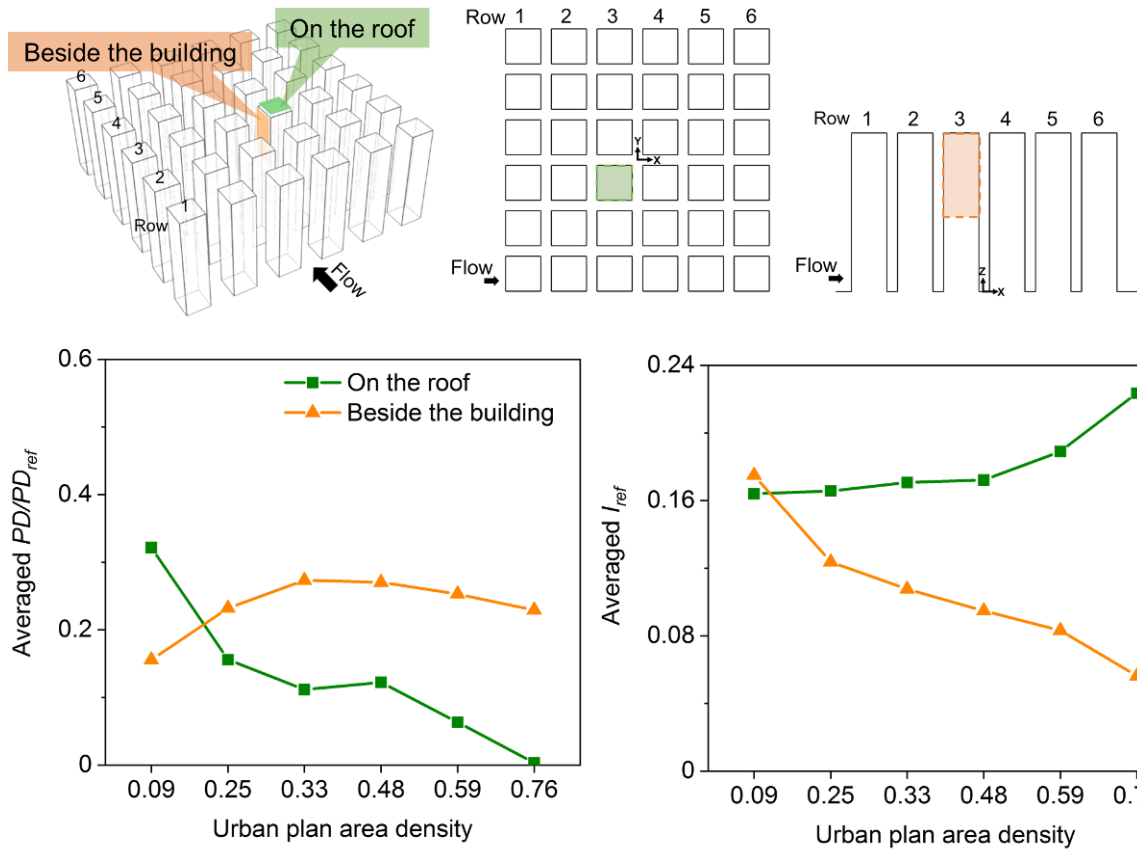


Figure 11 Predictions of average dimensionless power densities and average reference turbulence intensity of selected areas over the horizontal plane at $z/H= 1.03$ on the roof as well as the vertical plane at 1.5 m beside the building for varied urban plan area densities.

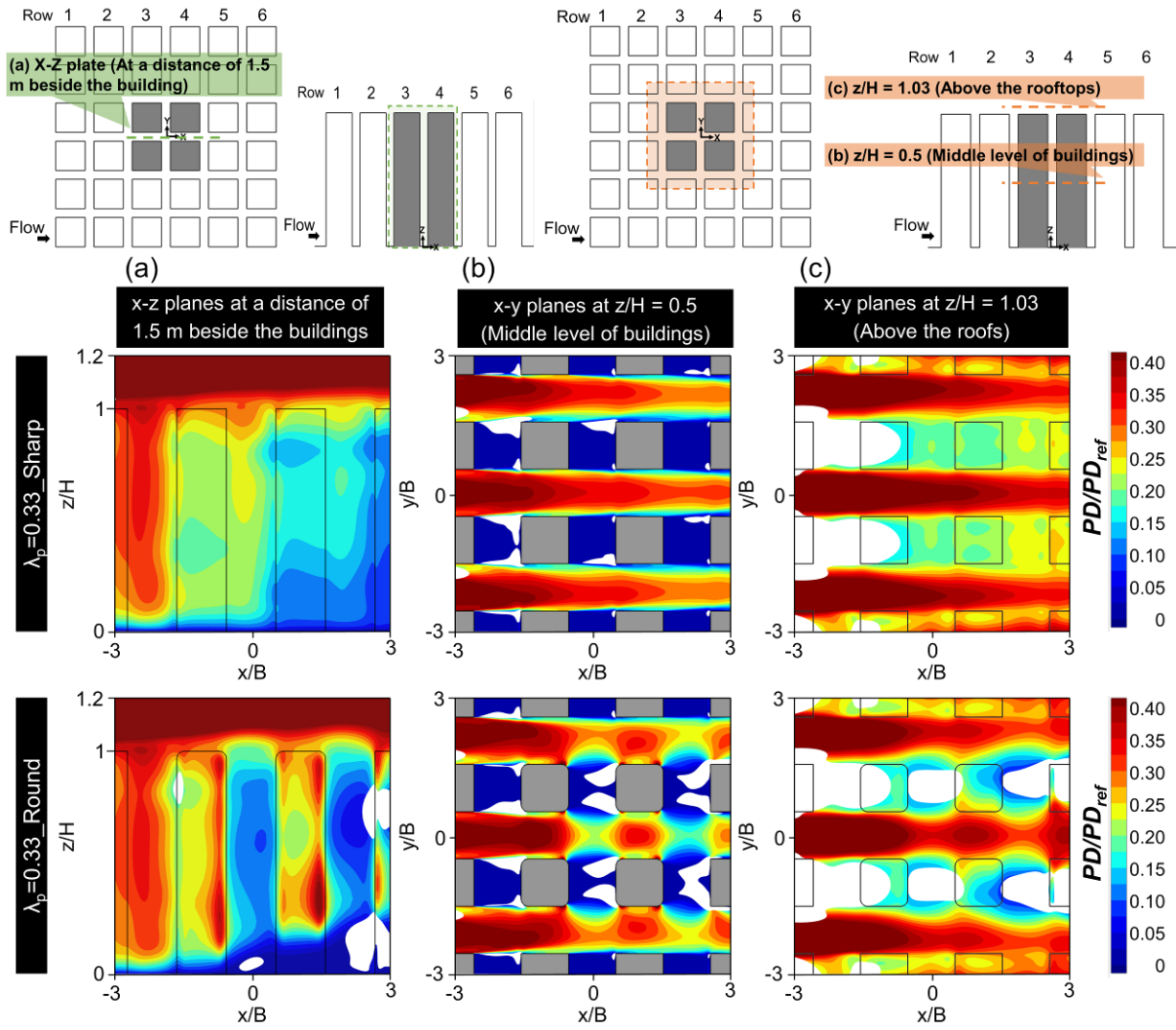


Figure 12 Predicted contour plots of dimensionless power density (with unacceptable turbulence region in white color) over the vertical x-z planes (a) at a distance of 1.5 m beside the buildings as well as the horizontal x-y planes (b) at $z/H = 0.5$ and (c) 1.03 for the sharp/round corners and urban layout of $\lambda_p = 0.25$.

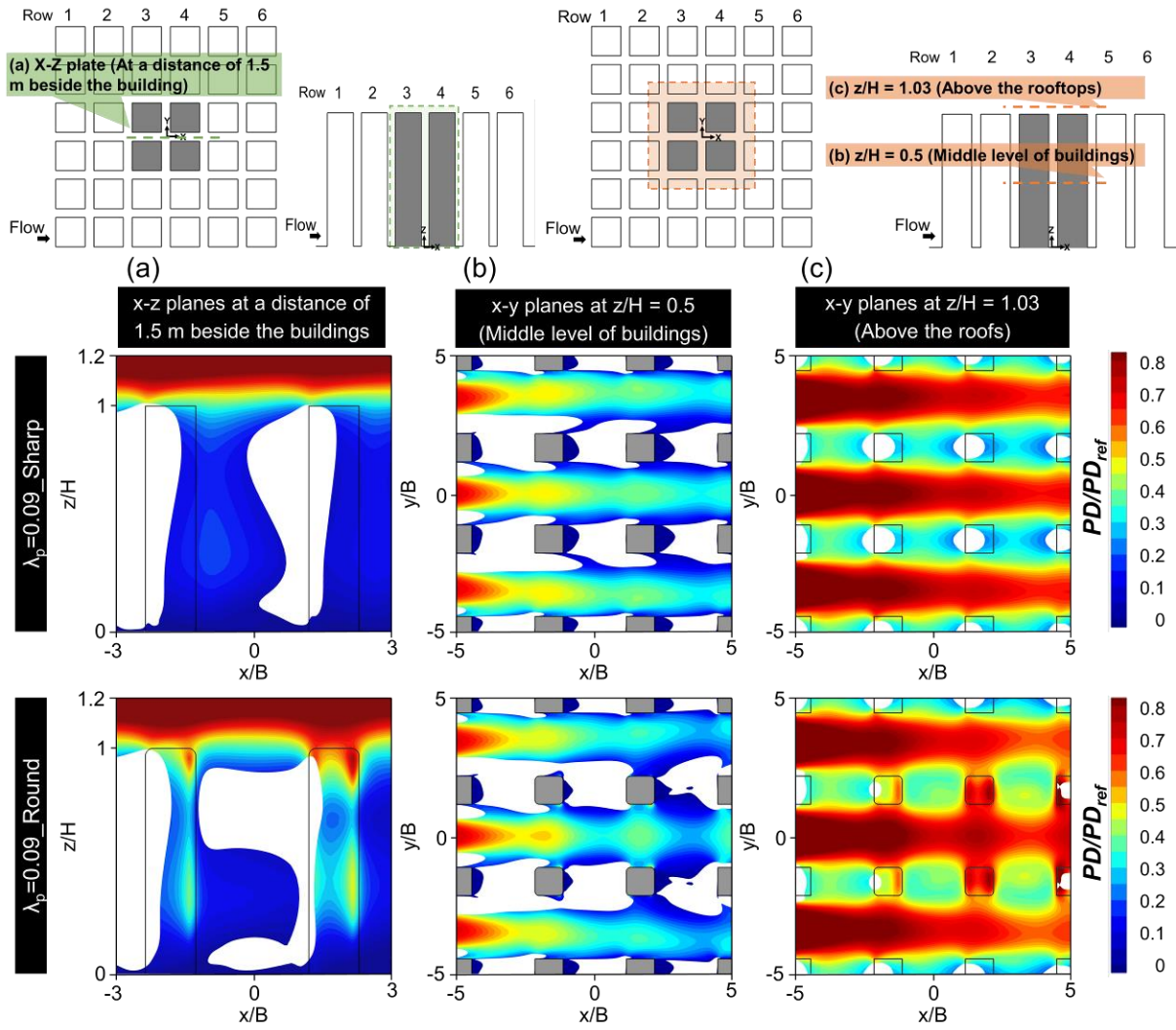


Figure 13 Predicted contour plots of dimensionless power density (with unacceptable turbulence region in white color) over the vertical x-z planes (a) at a distance of 1.5 m beside the buildings as well as the horizontal x-y planes (b) at $z/H = 0.5$ and (c) 1.03 for the sharp/round corners and urban layout of $\lambda_p = 0.09$.

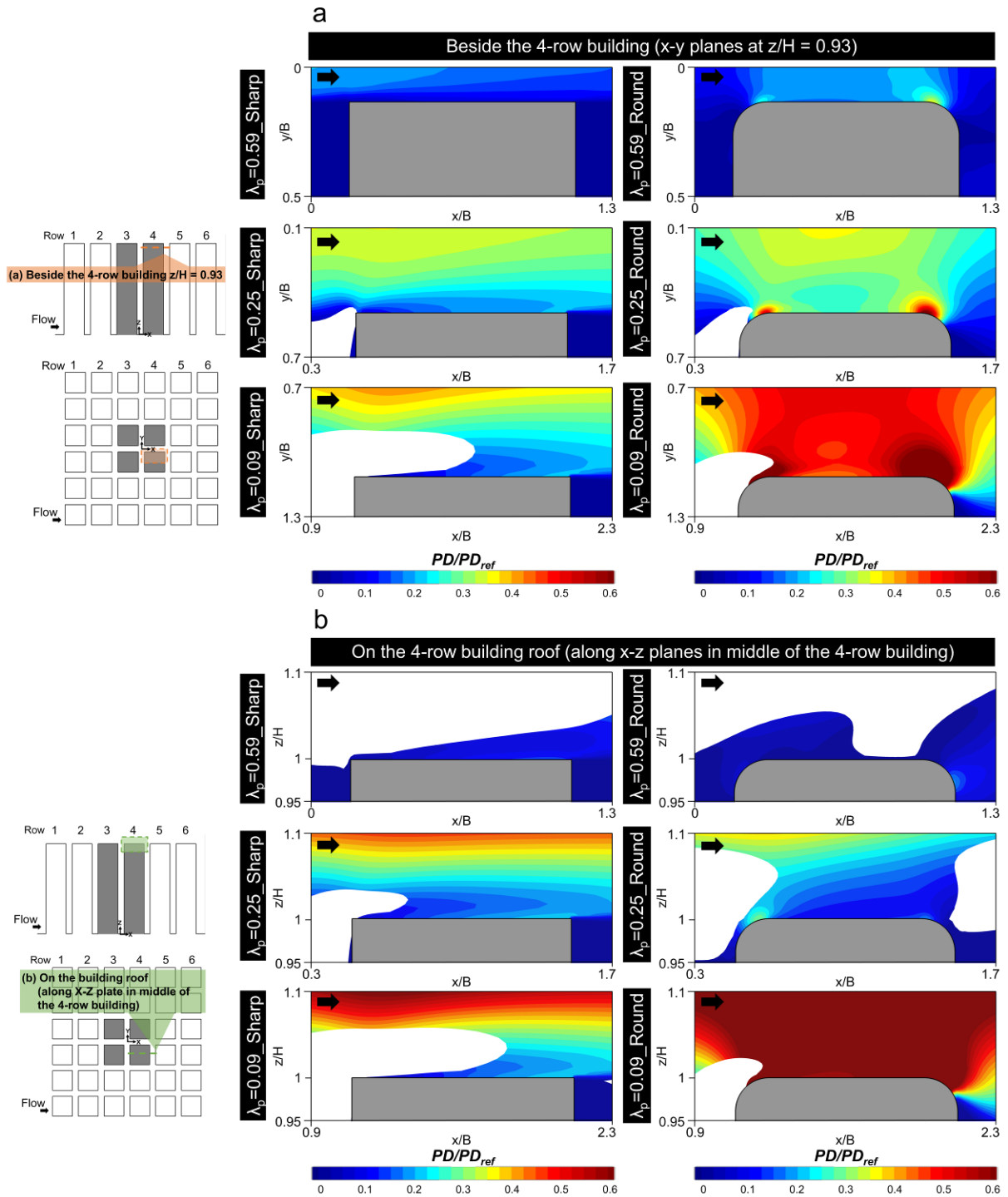


Figure 14 Predicted contour plots of dimensionless power density (with unacceptable turbulence region marked in white color) (a) beside the buildings over horizontal x-y planes at $z/H = 0.93$, and (b) on the roofs along vertical x-z planes in the middle of 4-row buildings for sharp/round corners and urban layouts of $\lambda_p = 0.09$, 0.25 , and 0.59 .

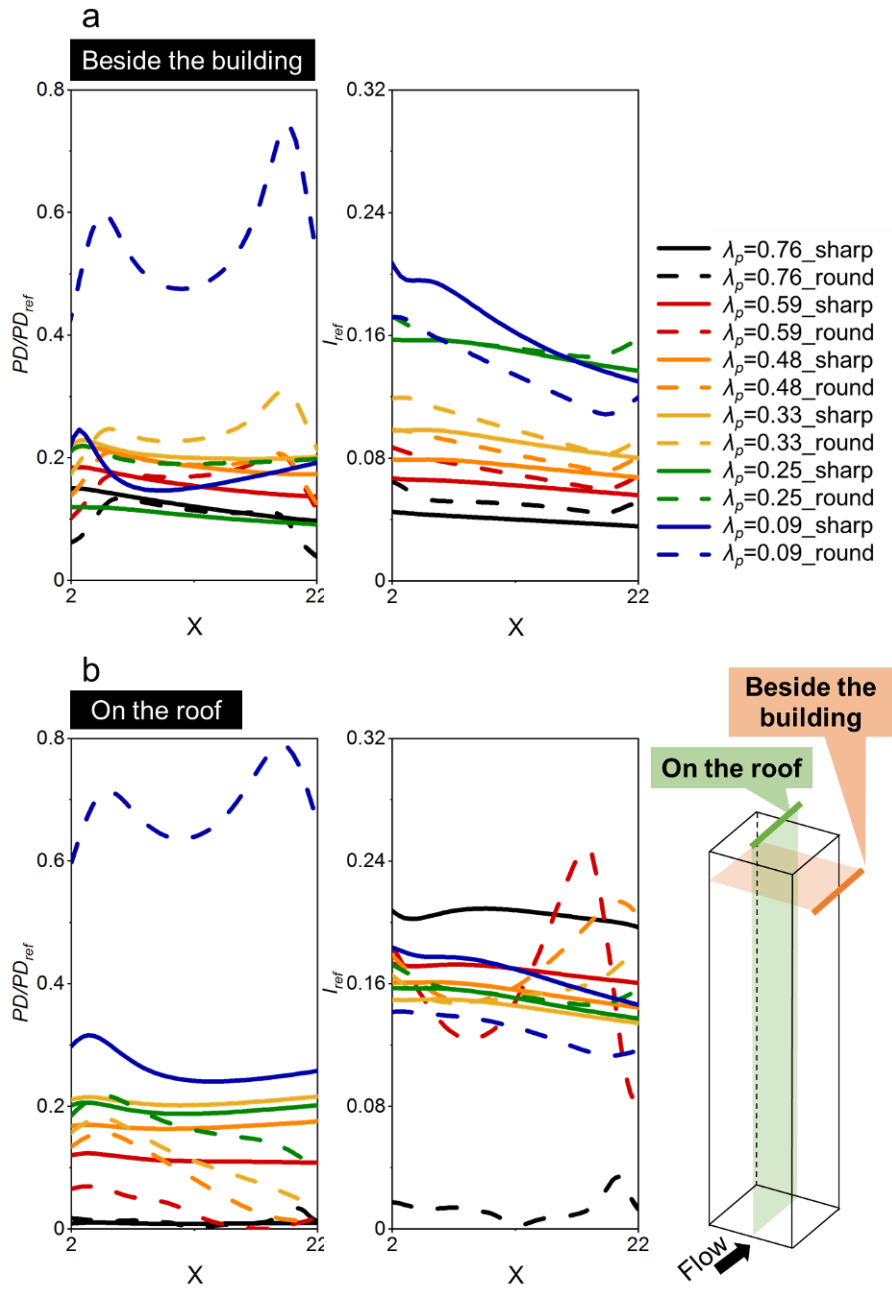


Figure 15 Predicted profiles of wind power density and reference turbulence intensity along building length of two selected areas (a) beside the building and (b) on the roof for sharp/round corners at varied urban densities.

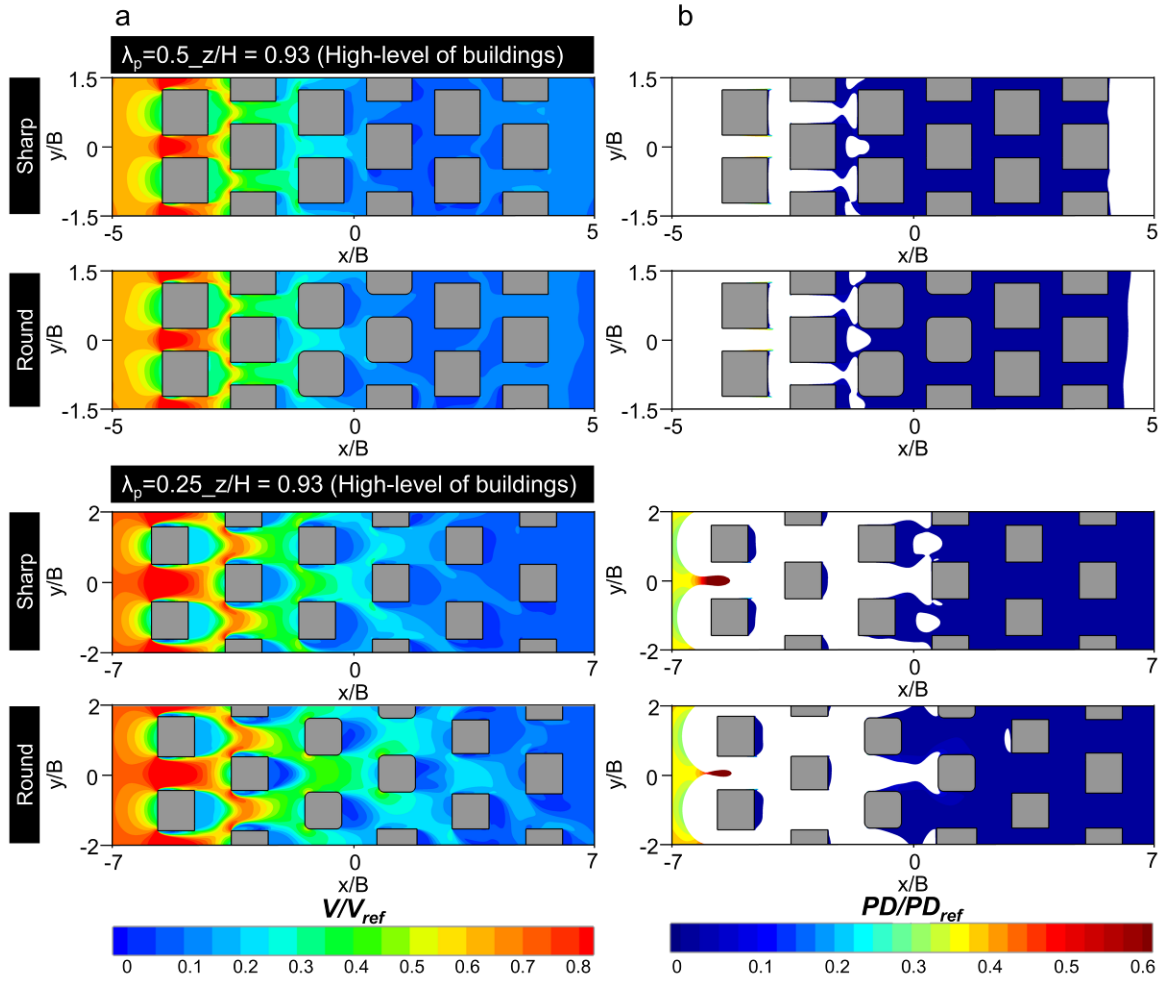


Figure 16 Predicted contour plots of (a) dimensionless velocity magnitude and (b) dimensionless power density (with unacceptable turbulence region marked in white color) over the horizontal x-y plane at $z/H=0.93$ for sharp/round corners and staggered urban layouts of $\lambda_p=0.25, 0.5$.

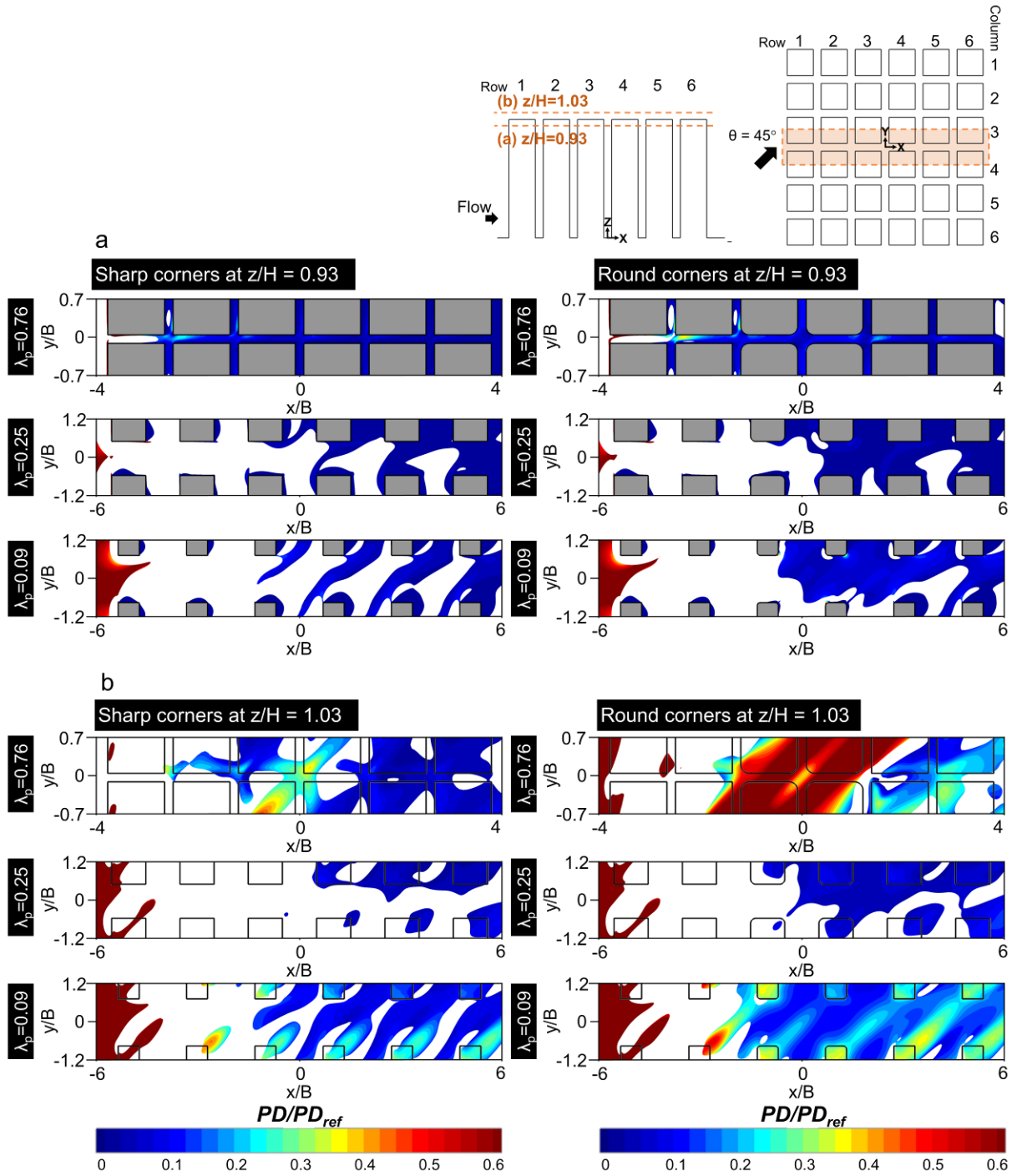


Figure 17 Predicted contour plots of dimensionless power density (with unacceptable turbulence region marked in white color) over horizontal x - y planes at (a) $z/H = 0.93$ and (b) 1.03 with wind direction of 45° for sharp/round corners and urban layouts of $\lambda_p = 0.09, 0.25, 0.76$.